Stony Brook University

Theoretical studies of metal/ferroelectric superlattices

A Thesis Presented

by

Judith Gabel

to

The Graduate School

in Partial Fulfillment of the

Requirements

for the Degree of

Master of Arts

in

Physics

Stony Brook University

August 2011

Stony Brook University
The Graduate School

Judith Gabel

We, the thesis committee for the above candidate for the Master of Arts degree, hereby recommend acceptance of this thesis.

Maria V. Fernandez-Serra - Thesis Advisor
Assistant Professor, Department of Physics and Astronomy

Matthew Dawber
Assistant Professor, Department of Physics and Astronomy

Philip B. Allen
Professor, Department of Physics and Astronomy

This thesis is accepted by the Graduate School.

Lawrence Martin
Dean of the Graduate School

Abstract of the Thesis

Theoretical studies of metal/ferroelectric superlattices

by

Judith Gabel

Master of Arts

in

Physics

Stony Brook University

2011

In this thesis $SrRuO_3/PbTiO_3$ superlattices are studied. Experimentally it is not known which interface forms when these structures are grown. We investigated the formation energy, the structural, electrostatic, magnetic and electronic properties of the different interfaces and compared our findings to measurements to determine the interface structure realized in experiments.
The dependence of the superlattices on strain and rotational distortions is also analyzed. For asymmetric interface structures we find an interesting phase diagram of the superlattices going from a ferroelectric material with an asymmetric double-well potential then via a self-poling polar structure to a paraelectric superlattice when the $PbTiO_3$ volume fraction is decreased.

Contents

List of Figures

List of Tables

Acknowledgements

First and foremost, I would like to thank my thesis advisor, Prof. Marivi Fernandez-Serra for her kind guidance during my research. Her assistance, stimulating suggestions and encouragement were an invaluable help in all the time of research and in writing this thesis.

I am also deeply grateful for many helpful discussions with Sara Callori and Prof. Matthew Dawber and for the experimental data provided by them.

Furthermore I want to thank Prof. Matthew Dawber and Prof. Philip B. Allen for serving on my thesis defense committee.

Last, I would like to acknowledge nine months of funding for this thesis provided by the German Academic Exchange Service (DAAD).

Chapter 1

Introduction

As fossil fuels cannot satisfy the energy demand of modern society, it is important to find regenerative replacements for fossil fuels. The largest source of regenerative energy is the sun. But the question arises of how to use and store the abundant energy coming from the sun.

One way to store the sun's energy is to use sun light to split water into hydrogen and oxygen. In the quest for suitable catalytic materials for solar water splitting ferroelectric materials seem like good candidates as their domain structure provides an automatic charge separation possibly facilitating catalytic reactions.

To split water efficiently the band gap of the catalyst has to match the energy of the most abundant solar photons which lies in the visible range at sea level.

The physical properties of ferroelectric materials can be tailored by building superlattice structures composed by different materials. Supercell structures thus seem suitable for bandgap engineering.

We study the promising SRO/PTO superlattices. Growing these materials it is not clear which interface structure forms. Due to the volatility of different atom species some interface terminations may be unstable and prohibit the growth of the structure in the originally intended stoichiometry and structure.

As the interface structure effects the physical properties of the superlattice, such as the polarization or the size of the bandgap, it is important to find out which interface structure forms experimentally.

By studying the energetics, the structural, electrostatic, electronic and magnetic properties and comparing them to experiment we try to determine the interface structure of the superlattices which is realized in experiments.

The thesis is organized as follows:

Chapter 2 introduces the density functional theory and the methods used in this thesis. Chapter 3 gives an overview of ferroelectricity and its treatment in density functional theory. In chapter 5 to 10 the energetics, structural, electrostatic, electronic and magnetic properties of the different ferroelectric structures are discussed. The influence of strain and rotations of the oxygen octahedra on the structures are analyzed in chapter 11 and 12.

Chapter 2

Methods

2.1 Density Functional Theory

Density functional theory (DFT) is a quantum mechanical method to calculate the ground state of a system of electrons and nuclei.

The Born Oppenheimer approximation [3] is used to decouple the movement of electrons and nuclei. As atomic nuclei are much heavier than electrons and thus move more slowly, they can be treated as fixed while calculating the electronic ground state. Using the electronic ground state the movement of the atoms can then be computed classically.

Density functional theory calculations [9] yield the electronic ground state: Using the uniqueness of the electronic ground state the Kohn-Sham ansatz converts the many-body system of interacting electrons described by the wave function $\psi(r_1, r_2...)$ into a set of non-interacting one-body wave functions $\{\psi_i(r)\}$. The Schrödinger equation describing the many-body system transforms under the Kohn-Sham ansatz to the one-particle Schrödinger equation

$$\left(-\frac{\nabla_i^2}{2} + V_{ext} + \int d^3r\prime \frac{n(r\prime)}{\mid r - r\prime \mid} + V_{xc}\right)\psi_i(r) = \epsilon_i\psi_i(r)$$

where the first term describes the kinetic energy of the one-particle orbitals and V_{ext} denotes the external potential. The third term is called Hartree term describing the electron-electron Coulomb repulsion. The fourth term is the exchange and correlation potential and includes all the many-particle interactions.

The exact form of the exchange and correlation functional is not known and many approximations were proposed to parametrize the exchange and correlation functional. In the next section we introduce the parametrizations of the exchange and correlation functional used in this study.

Using these parametrizations the one-particle Schroedinger equation can be solved iteratively to calculate the electronic ground state.

2.2 Exchange and Correlation Functional

In this study different parametrizations of the exchange and correlation functional were used:

The local density approximation [13] assumes that the exchange and correlation functional only depends on the local electron density. LDA works well for metals such as SRO and is also commonly used for

ferroelectric materials. The local spin-density calculation (LSDA) is a generalization of the local density approximation which includes the spin.

Generalized gradient approximations (GGA) of the exchange and correlation functional do not only take the electron density in account but also its gradient. The GGA parametrization of the exchange and correlation functional recently proposed by Wu and Cohen (WC) [28] is known to reproduce good structural parameters for ferroelectric materials and is also applied in this thesis.

It is well known that the band gap is typically underestimated in density functional theory calculations. This shortcoming is due to the incomplete cancellation of the self-interaction in the Hartree term and the exchange and correlation functional. To make up for this underestimation of the band gap and to reproduce experimental bandgaps we used an additional on-site Coulomb interaction U [14, 2, 7] (also called Hubbard term) when calculating the band structure for a structure which was previously relaxed in a LDA or GGA calculation.

In the next section, we explain how the polarization can be computed in density functional theory calculations.

2.3 Modern Theory of Polarization

The classical definition of the polarization as the dipole moment per unit volume can't be applied in DFT calculations of periodic crystals since the polarization defined this way depends on the unit cell which can't be chosen uniquely.

But one can nevertheless define a polarization in periodic systems. The modern theory of polarization [11] focuses on the change in polarization when switching between two different polarization states given by

$$\Delta P = \int_{\lambda_1}^{\lambda_2} \frac{\partial P}{\partial \lambda} d\lambda$$

where λ parametrizes the path between the two different polarization states. The change in polarization can be separated into an ionic and an electronic contribution. The ionic part can be calculated trivially. If the transformation along the path from λ_1 to λ_2 is adiabatic and the structure remains insulating along the whole path, one can rewrite the equation given above in electronic wave functions and use first-order perturbation theory to derive a well-defined equation giving the change in the electronic polarization [11].

As the superlattices studied in this thesis are metallic, we cannot calculate the polarization of the structures directly using the equations of the modern theory of polarization. Instead, we have to compute the so-called layer polarization [25] which makes use of the Born effective charges. The Born effective charges are tensorial dynamical charges describing the change in polarization if an atom is displaced in a certain direction.

Looking at the superlattice structures in the following chapters we find that they have bulk-like insulating layers with a polarization pointing in c direction. To calculate their polarization we pick one unit cell of the bulk-like layers of the superlattice and compute the Born effective charges of the atoms in this single unit cell in a separate calculation. Neglecting possible reordering of charges we then assume that the Born effective charges of the single unit cell calculation can be used for all atoms of the superlattice. Due to the symmetry of the superlattices the polarization is only non-zero in c direction and we can approximate the

dipole density p_j of layer j in the superlattice by multiplying the bulk Born effetive charges of the single unit cell with the atomic displacements in c direction occurring in layer j [25]:

$$p_j = \frac{1}{S} \sum_{\alpha \epsilon \text{layer j}} Z^*_\alpha R_{\alpha z}$$

In this equation S describes the horizontal area of the unit cell, $R_{\alpha z}$ denotes the displacement of atom α in c direction and Z^*_α are the Born effective charges in c direction for atomic displacement along c.

In perovskite materials the layer dipole density is ill-defined. The dynamical charges of the single layers do not fulfill the acoustic sum rule and do not add up to 0, thus making the dipole density origin dependent. To address this issue, the dipole density is averaged over several layers

$$\bar{p}_j = \frac{1}{4} p_{j-1} + \frac{1}{2} p_j + \frac{1}{4} p_{j+1}$$

Taking into account that a layer makes up half a unit cell the layer polarization reads

$$P_j = \frac{2}{c} \bar{p}_j$$

where c denotes the height of the unit cell in question.

The layer polarization has several shortcomings. It's only exact in the linear limit of small polar distortions. Besides, it does not take into account that the bulk unit cells are exposed to an electrical field which affects the polarization as well.

2.4 Macroscopic Averaging

We are usually interested in the behavior of quantities perpendicular to the interfaces of the superlattices. That's why we typically average quantities over the x and y direction. The so-called planar average $V(z)$ of e.g. the electrostatic potential $V(x, y, z)$ is then given by

$$V(z) = \frac{1}{S} \int_S V(x, y, z) dx dy$$

where S describes the horizontal area of the unit cell. The averaged quantity is still dependent on the microscopic structure of the material as quantities like the electrostatic potential or the charge density are strongly modulated by the atoms of the superlattice. To get rid of the atomic oscillations we apply the double macroscopic averaging technique [19, 10] where the planar averaged quantities are averaged in c direction with two step-like filter functions whose lengths correspond to the average length of a unit cell in c direction.

The averaging cancels the contributions of single unit cells and shows therewith the underlying macroscopic behavior of the considered quantity.

This technique can only be used in bulk structures where neighboring unit cells are similar to each other and the atomic contributions from different unit cells can cancel each other. In interfacial layers one always finds a superposition of the atomic variations and the underlying macroscopic behavior of the quantity.

2.5 Technicalities

The first principles calculation were performed using a numerical atomic orbital method, as implemented in the SIESTA code [24].

Core electrons were replaced by fully-separable [12] Troullier-Martin [26] pseudopotentials. Details on the basis set and pseudopotentials used can be found in Ref. [10].

For the local density approximation (LDA) [13] the Perdew-Zunger [18] parametrization of Ceperley-Alder [5] data was used. In the generalized gradient approximations (GGA) we made use of the parametrization of the exchange and correlation potential as proposed by Wu and Cohen (WC) [28]. To improve the description of electronic properties we performed LDA+U calculations using an effective Hubbard parameter U as proposed by Dudarev [7].

In $\vec{k}$-space a sampling was used that corresponds to $6 \times 6 \times 6$ Monkhorst-Pack mesh [15, 16] for a single bulk unit cell of the perovskite. For the materials in which the metallic contribution was high a finer k point mesh corresponding to a $12 \times 12 \times 12$ and a $16 \times 16 \times 16$ Monkhorst-Pack mesh for a single perovskite bulk unit cell was used. For calculations of the projected and local density of state the mesh of the reciprocal space was further refined.

Real space integrations were performed using an uniform real-space grid with an equivalent plane-wave cutoff of 400 Ry.

Structures were relaxed until the maximal force component fell below 0.025 eV/Å and the maximal stress component fell below 1GPa respectively.

Chapter 3

Ferroelectrics

3.1 Perovskite Oxides

Many oxides with a ABO_3 composition crystallize in a perovskite structure which is shown in figure 3.1. In the ideal perovskite structure the cation A sits at the origin of the unit cell at $(0, 0, 0)$. Cation B is positioned at the center of the unit cell at $(\frac{1}{2}, \frac{1}{2}, \frac{1}{2})$ and the oxygen atoms sit at face-centered positions at $(\frac{1}{2}, \frac{1}{2}, 0)$, $(\frac{1}{2}, 0, \frac{1}{2})$ etc. forming an octahedron. The unit cell layers in perovskite crystals thus have alternatingly a AO and a BO_2 composition.

The materials studied in this thesis all have a a ABO_3 composition:

$SrTiO_3$(STO) has a cubic perovskite structure and is paraelectric at room temperature. The experimentalists use it as an substrate to grow their metal/ferroelectric films on it as it has a small lattice mismatch with the materials composing the superlattice they want to grow[21].

$SrRuO_3$ (SRO) is a metal with an orthorhombic crystal structure at room temperature. But grown on a STO substrate SRO also crystallizes in a perovskite structure [29].

$PbTiO_3$ (PTO) is a ferroelectric with a perovskite structure at room temperature [8, 6]. Ferroelectrics are structures which exhibit a spontaneous polarization, i.e. a non-zero, switchable electric polarization in zero electrical field. Ferroelectricity in PTO is induced by displacements of the oxygen octahedra and the B cation in vertical direction as shown by the arrows in figure 3.1. The polarization points against the direction of the displacement of the oxygen octahedra and the B cation. The polarization of the PTO unit cell in figure 3.1 would thus point downwards.

Energetically, ferroelectrics are described by a double-well potential, as shown in figure 3.2 [20]. The potential has two equal energy mimina in which the system has equal and opposite polarization. These configurations are more stable than the non-polar structures.

At high temperatures PTO becomes paraelectric crystallizing in the ideal cubic perovskite structure [6].

3.2 Superlattices

The structures analyzed in this thesis are layered superlattices. Planes of SRO and PTO unit cells are periodically stacked in c direction. Side views of some superlattice structures are shown in figure 4.1.

We give now some definitions of important quantities of the superlattices which are used throughout the thesis.

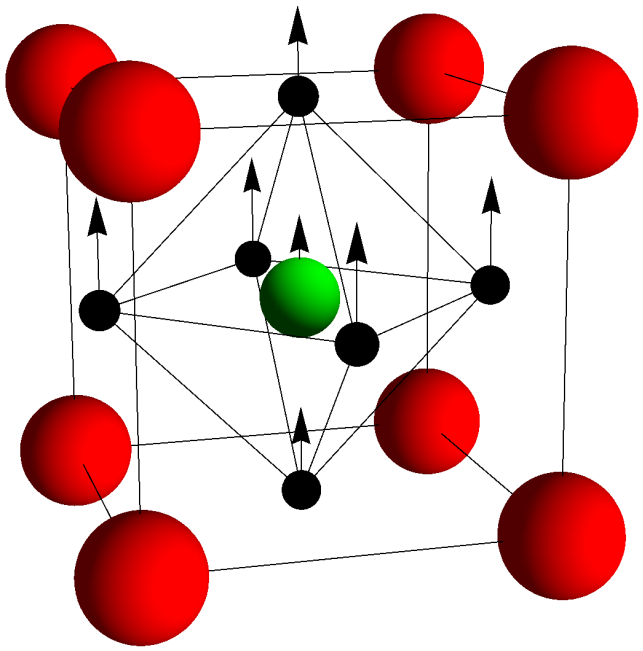

Figure 3.1: Cubic perovskite crystal structure. Red spheres symbolize cation A, green spheres cation B and black spheres the oxygens.The arrows show the direction of the ferroelectric distortion in PTO.

The PTO volume fraction VF(PTO) of a superlattice is defined as the number $\#_{\text{PTOunit cells}}$ of PTO unit cells in the superlattice divided by the total number $\#_{\text{unit cells}}$ of single perovskite unit cells in the superstructure:

$$\text{VF(PTO)} = \frac{\#_{\text{PTOunit cells}}}{\#_{\text{unit cells}}}$$

The average tetragonality $\frac{c}{a}$ of a superlattice is defined as the average height of the single perovskite unit cells in the superlattice given in units of the in-plane lattice constant a.

The layer rumplings describe the distance between the oxygen atoms and the A/B cations in the single layers.

3.3 Improper Ferroelectricity

Growing superlattices out of different materials the resulting structures are sometimes not built alike the unit cells of the original materials but entirely new ground states can arise.

The authors of [4] e.g. demonstrate that ferroelectric/paraelectric $PbTiO_3$/ $SrTiO_3$ superlattices with very short periods display not only a ferroelectric distortion in the tetragonal regime, but also improper ferroelectricity caused by rotations of the oxygen octahedra.

Figure 3.3 shows schematically the atomic motions associated to the antiferrodistortive distortions which give rise to improper ferroelectricity. The modes are distinguished by the direction of the oxygen rotations. If successive oxygen octahedra along the c direction are rotated in the same directions, the energy-lowering

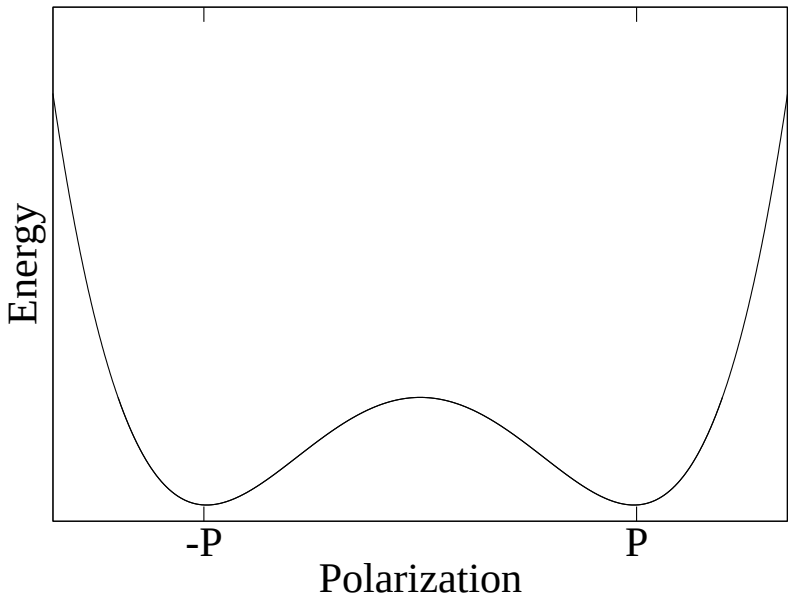

Figure 3.2: Double-well potential of a ferroelectric material

mode is called AFD_{zi} mode (in phase rotation). If successive oxygen octahedra along the c axis are rotated in opposing directions, the distortive mode is called AFD_{zo} (out of phase rotation). These antiferrodistortive modes decrease the rumplings and the polarization in c direction.

Tiltings of oxygen octahedra can as well reduce the total energy and the polarization.

3.4 Sputter Deposition

The structures considered in this thesis are grown using the sputter deposition technique[20].

The films are grown in a vacuum chamber filled with sputtering gas (e.g. Ar). The sputtering gas is accelerated towards the target material, which is a ceramic with the same stoichiometric composition as the desired film. The highly energetic particles of the sputtering gas hit the target and eject atoms from the surface of the target. If an oxide films is grown, the vacuum chamber is not only filled with the plasma but also with oxygen. Atoms ejected from the target and oxygens reach the substrate (in this study $SrTiO_3$), which is heated to the so-called growing temperature, where they are deposited.

To build an artificial superlattice the experimentalists calibrate the growing rates and times of the atoms composing the different unit cells. They then alternately grow the different unit cells in the proportionality of the superlattice they want to build.

3.5 Ferroelectrics in Density Functional Theory

The typical underestimation of the band gap in DFT calculations can lead to pathological regimes when studying metal/ferroelectric interfaces [25]:

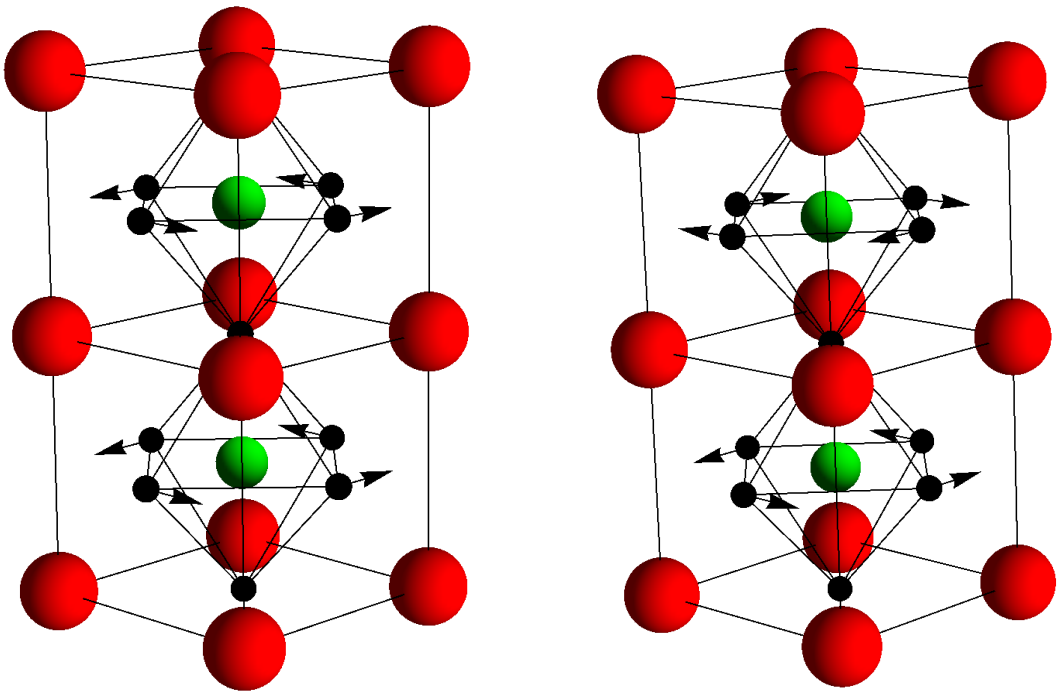

(a) (b)

Figure 3.3: Schematic view of antiferrodistortive modes (a) shows the AFD_{zi} mode (b) shows the AFD_{zo} mode

The metallic layers try to screen the surface charges of the ferroelectric unit cell. But this screening is imperfect resulting in uncompensated charges at the metal/ferroelectric interface which generate an electric depolarizing field. If the drop in electrostatic potential caused by the electric field is larger than the underestimated bandgap, charges of the conduction bands are artificially spilled out and can lead in consequence to the development of a pathological regime in the relaxation calculations. Thus one has to check carefully that the depolarizing field of the structures is not strong enough to cause such a pathological regime.

The superlattices are simulated using a supercell approximation with periodic boundary conditions. Through the use of periodic boundary conditions short-circuit periodic boundary conditions are imposed.

To account for the mechanical boundary conditions imposed by the $SrTiO_3$substrate used in the experiments the in-plane lattice constant a of the superlattices was strained to the theoretical in-plane lattice constant of $SrTiO_3$. For the LDA and LSDA calculations we calculated an in-plane lattice constant for STO of $a = 3.87$Å, for the WC calculations we computed an in-plane lattice constant for STO of $a = 3.905$Å. The out-of-plane lattice vector is allowed to relax freely.

Unless otherwise noted, the structures were constrained to their ideal tetragonal state: A (1×1) periodicity is used in the plane perpendicular to the c axis. The atomic positions are fixed to the x and y position imposed by the mirror symmetry of the perovskite unit cells in x and y direction. Only relaxations in c direction are allowed. The forces in c direction acting upon symmetrically equivalent atoms (e.g. the O atoms in the BO_2 plane) are furthermore symmetrized so that the symmetrically equivalent atoms are

pinned to the same c coordinate.

The calculations of the superlattices were started using an initial configuration corresponding to a ferroelectric distortion of the PTO layers. For structures in which the two polarization states are not equivalent we performed calculations starting from the initial configuration of either polarization direction and compared their total energy to find the ground state.

To allow rotations of the oxygen octahedra, the in-plane size of the supercell has to be doubled [4]. The oxygen octahedra were then allowed to rotate around the c axis. All the other atoms were still constrained to their ideal tetragonal positions. Forces acting on symmetrically equivalent atoms in c direction were still symmetrized.

For the calculations including rotations we chose initial positions corresponding to a ferroelectric configuration upon which in-phase and out-of phase rotations of the oxygen octahedra were added.

In the next chapter we describe the superlattice structures studied in this thesis.

Chapter 4

Interface Structure

The structures considered in this thesis are grown using the sputter deposition technique as described in Section 3.4. To build a superlattice the experimentalists alternately grow the different layers in the proportionality of the superlattice they want to build. The structures are grown on a STO substrate which ends in TiO_2 planes. Assuming well-controlled growth rates, one could imagine that layer by layer is deposited with each layer ending in a BO_2 composition. But depending on the diffusivity of the atoms the surface termination of the different layers can change, resulting in different interface structures.

It is e.g. known that Ru is very volatile: When growing SRO on TiO_2 terminated STO by pulsed laser deposition at 700°C, the surface termination changes from a BO_2 (i.e. RuO_2) termination to a AO (i.e. SrO) termination within one unit cell. At lower temperatures the change in surface termination occurs within the growth of several unit cells [22].

But as most of the structures considered in this thesis only contain a single unit cell of SRO and the experimentalists use a small growing temperature (550°C) due to the high volatility of Pb, it is not clear if the termination conversion already occurs in these systems. Furthermore the structures are grown using sputter deposition instead of pulsed laser deposition. The different kinetic regime could also influence the termination conversion and thereby the interface formation.

Keeping the perovskite structure intact, in which the planes have alternately either a AO or a BO_2 composition, one can think of three possible interface structures. Type 1 is an asymmetric superlattice with two different interfaces. This composition of the stucture corresponds to the proportionality of the growth rates and growth times used experimentally. In this case the SRO layer would terminate in a SrO plane at one interface and in a RuO_2 plane at the other interface. On the other hand, one could also imagine to find a symmetric structure of the interfaces. The SRO layer could end in either only SrO planes or in only RuO_2 planes.

Side views of the three different interface structures are illustrated in figure 4.1. We denote all superlattices by the composition of the corresponding asymmetric structure. A $(SRO)_1(PTO)_5$ superlattice can e.g. stand for an asymmetric superlattice or a symmetric superlattice with SrO-terminated SRO, which actually has a $(STO)_1(PTO)_4(SRO)_1$ composition, or a symmetric superlattice with RuO_2-terminated SRO with a $(STO)_1(PTO)_4(PRO)_1$ composition.

It is not clear which of these interface structures is realized experimentally. In the next chapter we thus try to find the theoretically most stable structure by calculating the formation energy of the different

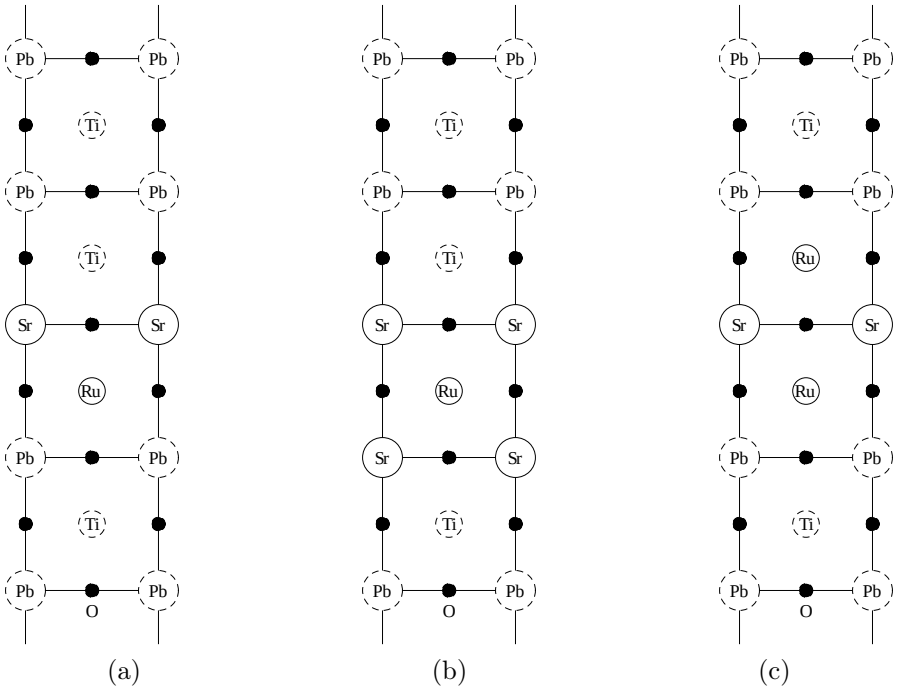

Figure 4.1: Side views of the different interface structures. (a) shows the asymmetric interface structure where the SRO layer ends in two different atomic planes. (b) and (c) show the structures with a symmetric interface. (b) illustrates the structure in which the SRO layer terminates only in SrO planes. In the structure depicted in (c) the SRO layer terminates only in RuO_2 planes.

superlattices.

Chapter 5

Formation Energy

The symmetric and asymmetric structures described above do not have the same number of atoms of each species. To find the most stable structure one therefore cannot compare the total energies directly, as the total energy strongly depends on the total energy of the single components of the superlattice.

Instead, we define the formation energy which takes into account the differences in superlattice composition and subtracts the contribution of the superlattice components from the total energy of the superlattice.

For a superlattice composed of n single perovskite unit cells the formation energy is given by

$$E_{\text{formation}}\,(\text{superlattice}) = E_{\text{total}}\,(\text{superlattice}) - \sum_{\text{unit cell}=1}^{n} E_{\text{total}}\,(\text{unit cell})$$

where $E_{\text{total}}\,(\text{superlattice})$ describes the total energy of the whole superlattice and $E_{\text{total}}\,(\text{unit cell})$ describes the total energy of the single unit cells composing the superlattice. The total energy of a single unit cell is computed in a bulk relaxation calculation of this unit cell restricted to the same symmetry and strain conditions as the superlattice.

Using the above definition, the formation energy of the $(\text{SRO})_1(\text{PTO})_5$ superlattice is e.g. given by

$$E_{\text{formation}}\,((\text{SRO})_1(\text{PTO})_5) = E_{\text{total}}\,((\text{SRO})_1(\text{PTO})_5) - E_{\text{total}}\,(\text{SRO}) - 5E_{\text{total}}\,(\text{PTO})$$

In the following sections, we always compare the formation energy of the symmetric structures to the formation energy of the corresponding asymmetric structure. Accordingly, the difference in formation energy $\Delta E_{\text{formation}}$ is defined as

$$\Delta E_{\text{formation}} = E_{\text{formation}}(\text{symm. structure}) - E_{\text{formation}}(\text{asymm. structure})$$

If this difference in formation energy is positive (negative), the formation energy of the asymmetric structure is lower (higher) than the formation energy of the corresponding symmetric structure and the structure with the asymmetric interface should be more (less) stable than the structure with the symmetric interface.

5.1 Symmetric Structure with SrO-terminated SRO

For a LDA, LSDA and WC parametrization of the exchange and correlation functional we compare the formation energy of symmetric superlattices with SrO-terminated SRO layers to the formation energy of the

Structure	$\Delta E_{\text{formation}}$[eV] LDA calculation	$\Delta E_{\text{formation}}$[eV] LSDA calculation	$\Delta E_{\text{formation}}$[eV] WC calculation
$(SRO)_1(PTO)_2$	-0.020	-0.021	-
$(SRO)_1(PTO)_3$	-0.014	-0.023	-0.039
$(SRO)_1(PTO)_5$	+0.009	+0.009	+0.006
$(SRO)_1(PTO)_6$	+0.035	-	-
$(SRO)_1(PTO)_7$	+0.063	+0.067	+0.059
$(SRO)_1(PTO)_9$	+0.096	-	-
$(SRO)_2(PTO)_5$	-0.022	-	-
$(SRO)_2(PTO)_9$	+0.056	-	-
$(SRO)_4(PTO)_1$	+0.006	-	-

Table 5.1: Formation energy of symmetric superlattices with SrO-terminated SRO layers compared to formation energy of corresponding asymmetric superlattices for different parametrization of the exchange and correlation functional

corresponding asymmetric superlattices in table 5.1. For structures with a high PTO volume fraction the asymmetric interface structure is more stable than the symmetric interface structure with SrO-terminated SRO layers. But as the volume fraction goes down, the difference in formation energy decreases and for a PTO volume fraction of 0.75 the symmetric structure becomes the more stable structure. If the volume fraction of PTO decreases even further so that the superlattices consist of more SRO unit cells than PTO unit cells the asymmetric structure again becomes more stable than the symmetric structure. These results are independent of the exchange and correlation functional used.

But some of the differences in energy are quite small and lie below the range of our computational accuracy. Especially for the superlattices with few unit cells of PTO one therefore cannot say if the conclusions drawn from the difference in formation energy hold for the experimentally formed interfaces.

5.2 Symmetric Structure with RuO_2-terminated SRO

Structure	$\Delta E_{\text{formation}}$[eV] LDA calculation
$(SRO)_1(PTO)_2$	+0.057
$(SRO)_1(PTO)_3$	+0.040
$(SRO)_1(PTO)_5$	+0.077
$(SRO)_1(PTO)_6$	+0.081
$(SRO)_4(PTO)_1$	+0.106

Table 5.2: Formation energy of symmetric superlattices with RuO_2-terminated SRO layers compared to formation energy of corresponding asymmetric superlattices for a LDA parametrization of the exchange and correlation functional.

In table 5.2 the formation energy of asymmetric structures is compared to the formation energy of symmetric superlattices with RuO_2 terminations of the SRO layers using the LDA approximation. One finds that the asymmetric structure yields the lower formation energy for all the considered structures. For structures with few PTO unit cells the asymmetric structure becomes less favored but the asymmetric structure still remains the most stable structure. The differences in formation energy are quite large. In agreement with the experimentally measured high volatility of Ru one can thus conclude that sole RuO_2

terminations of the SRO layers do not seem to be stable.

Concluding we saw that symmetric interfaces with RuO_2-terminated SRO layers are theoretically less stable than the asymmetric interfaces. For high PTO volume fractions the symmetric interfaces with SrO-terminated SRO layers are also less stable than the asymmetric interfaces.For intermediate PTO volume fractions the symmetric superlattices with SrO-terminated SRO layers become the most stable structure.

However, as the differences in energy are not large, the conclusions drawn from the differences in formation energy are not very reliable. In the next chapters we thus look separately at different characteristics of the symmetric and the asymmetric structure to see which structure is realized experimentally.

Chapter 6

Structural Properties

In the following sections we analyze the properties of the superlattices in an ideal tetragonal structure. This means that we impose a mirror symmetry in x and y direction and only relaxations in c direction are allowed. Furthermore the forces in c direction acting upon the symmetrically equivalent oxygen atoms in the oxygen octahedra are symmetrized so that the symmetrically equivalent O atoms have the same c coordinate.

To analyze the superlattices we compare the layer rumplings and the average tetragonality of the different structures.

The A$-$O (B$-$$O_2$) rumplings are defined as the distance between the A(B) cations and the oxygens in the single layers. The average tetragonality $\frac{c}{a}$ describes the average height of a single perovskite unit cell in the superlattices.

6.1 Asymmetric Structure

The asymmetric interfaces break the inversion symmetry of the superlattice. Thus each structure has two distinct polarization states which are not equivalent to each other in their structural and electrostatic properties and energy. The polarization state that yields the lower energy is denoted by P_+ . In Section 8.1 we will show that the P_+ ground state always displays a polarization pointing from the RuO_2 interface to the SRO interface. The structure with the polarization pointing from the SrO to the RuO_2 termination state is denoted by P_-.

In the following, when we do not explicitly look at both polarization states, we only consider the ground state structure with the polarization P_+.

6.1.1 Rumplings

The layer rumplings for some sample structures are shown in figure 6.1 for LDA calculations and in figure 6.2 for WC calculations.

For both choices of the exchange and correlation potential we find that for SRO-rich structures the rumplings in the PTO layers are very small, which corresponds to a paraelectric state of the PTO layers. In contrast, the rumplings of PTO layers in PTO rich structures become large and uniform implying that the PTO layers are ferroelectric.

Including the spin in LDA calculations barely changes the rumplings in structures with only one SRO unit cell. In structures with more SRO unit cells the rumplings change, in the magnetic SRO layers and in the

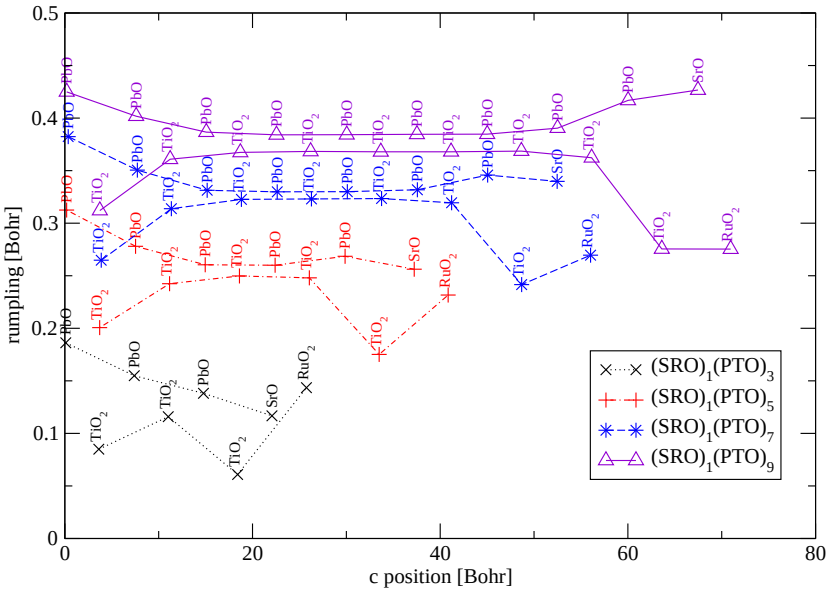

Figure 6.1: Layer rumplings for some asymmetric structures. The relaxation calculations were performed using the LDA approximation.

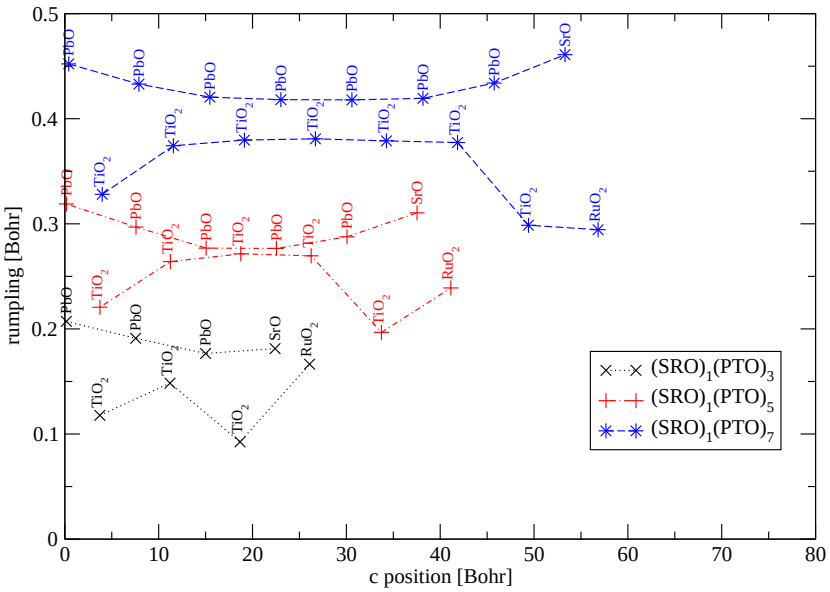

Figure 6.2: Layer rumplings for asymmetric structures. The atomic positions were relaxed using the WC GGA approximation.

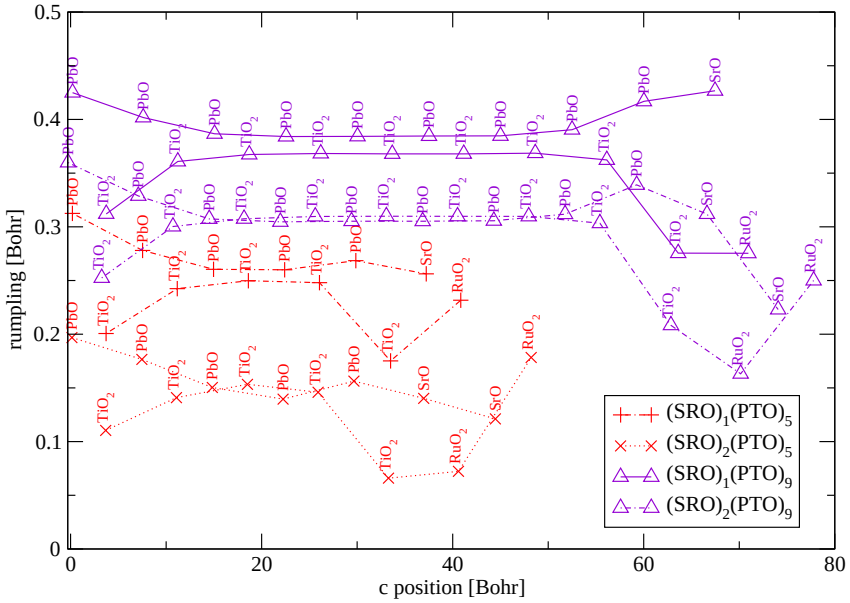

Figure 6.3: Comparison of layer rumplings for asymmetric superlattices with the same number of PTO unit cells and 1 or 2 unit cells of SRO. LDA calculation

interface layers, but also in the originally non-magnetic PTO layers, as shown explicitly for $(SRO)_2(PTO)_9$ in figure 6.4.

Using a WC exchange and correlation functional the rumplings become more pronounced as typically observed for this exchange and correlation functional.

The rumplings also change with the number of SRO unit cells as shown in figure 6.3 for some sample structures. When the number of SRO unit cells increases, the magnitude of the rumplings decreases. The polarization, being coupled to the rumplings of the layers, reduces as well.

6.1.2 Average Tetragonality

The average tetragonality $\frac{c}{a}$ of the single unit cells also depends on the PTO volume fraction as illustrated in figure 6.5.

Figure 6.5 shows the experimentally measured tetragonality [1] and the results of the first principles calculations for $\frac{c}{a}$ computed in LDA, spin polarized LDA and WC calculations.

In the theoretical calculations we see that there are sudden jumps in the tetragonality. These jumps occur when we relax structures with a very similar PTO volume fraction but a different number of SRO unit cells. Screening and polarization depend on the number of the metallic SRO unit cells as shown below in Section 8. Rumplings and especially tetragonality are themselves dependent on polarization. Thus the tetragonality changes abruptly when the number of SRO unit cells is changed.

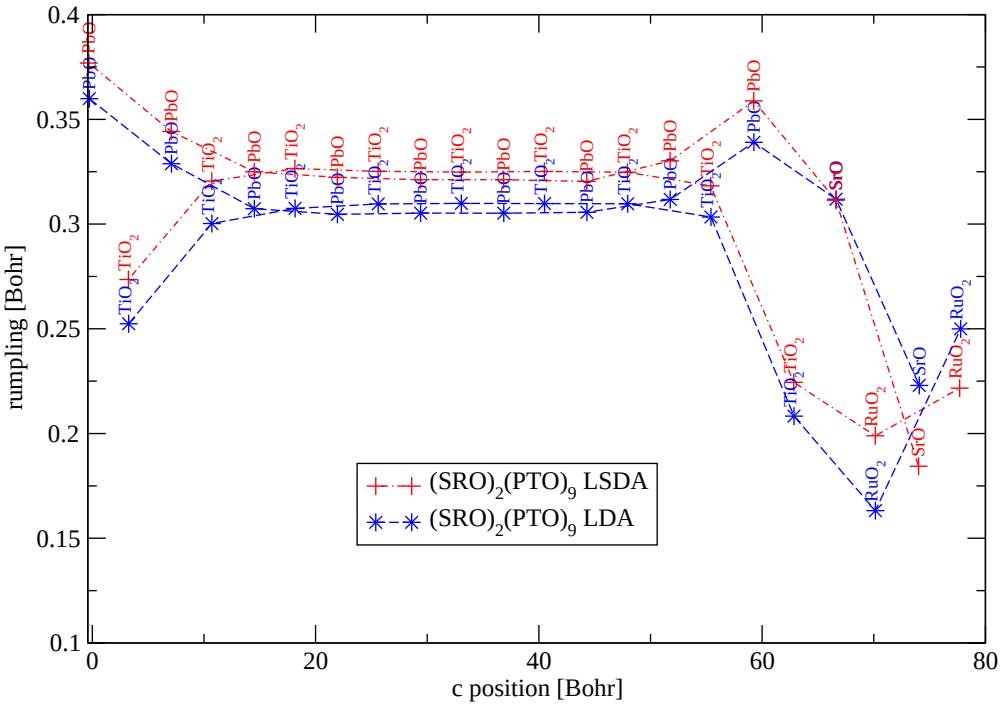

Figure 6.4: Rumplings for $(SRO)_2(PTO)_9$ structures in spin polarized and non spin polarized LDA calculations

Comparing the results for the different parametrizations of the exchange and correlation functional one finds that the general behavior of the average tetragonality is similar.

If the spin is included in the calculations, the tetragonality $\frac{c}{a}$ changes only slightly for PTO rich structures as the spin barely influences the tetragonality of the PTO layers and only changes the height of the SRO layers which only make up a small contribution of the total unit cell. But for SRO rich structures the spin inclusion changes the average tetragonality $\frac{c}{a}$ significantly.

Calculations with the WC exchange and correlation potential increase the differences in tetragonality $\frac{c}{a}$ between states with a similar PTO volume fraction but a different number of SRO unit cells. This behavior can be explained by the characteristics of the WC exchange and correlation potential. In calculations using the WC exchange and correlation potential rumplings and polarization are more pronounced than in LDA calculations. Changes in screening thus cause a larger change in the polarization and the tetragonality, resulting in larger differences in tetragonality if the number of SRO unit cells changes.

In every calculation one notices a dip in the tetragonality. Using the conclusions drawn from the rumplings one can understand this behavior.

Analyzing the rumplings we found that for SRO rich structures the PTO layers become paraelectric whereas they remain ferroelectric for PTO rich structures. The out-of-plane lattice constants of SRO,

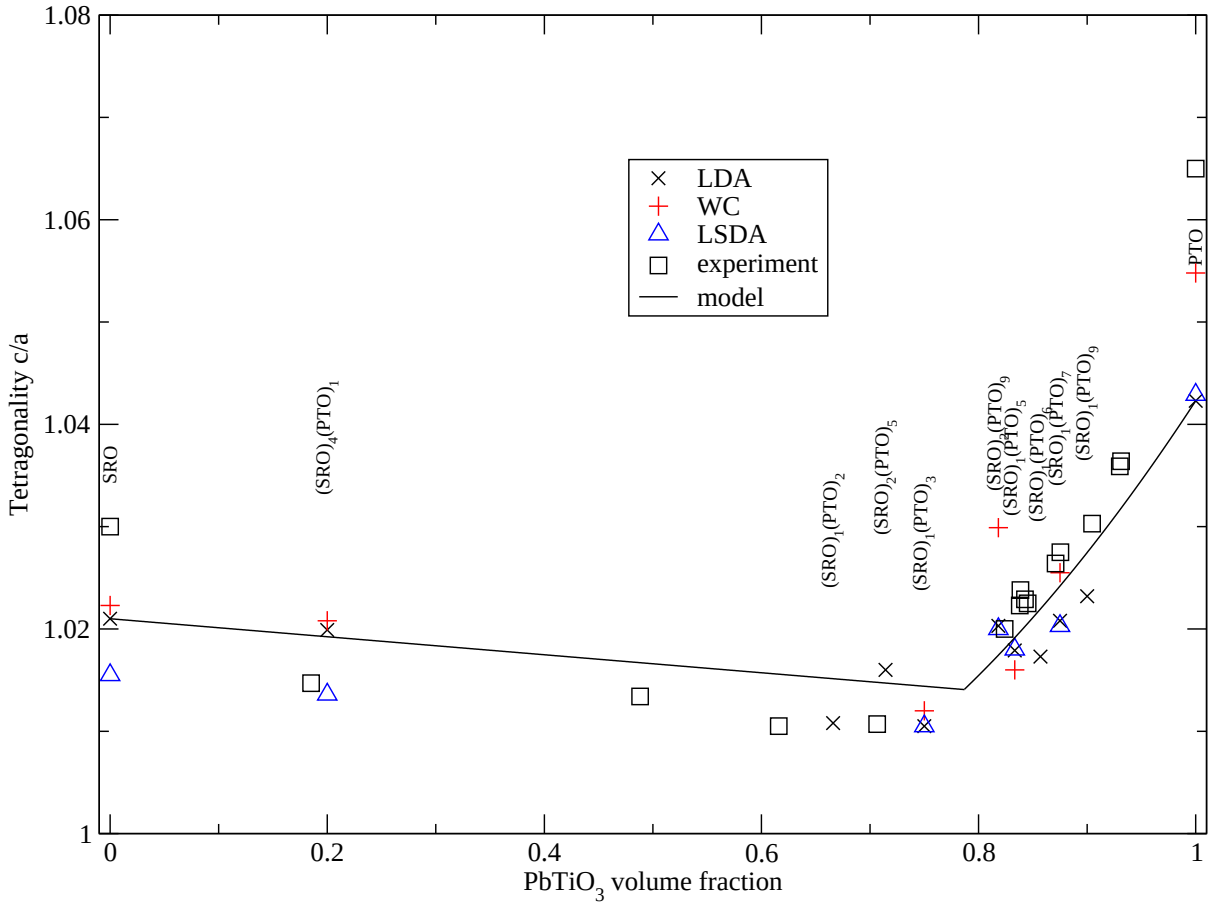

Figure 6.5: Average tetragonality $\frac{c}{a}$ of asymmetric superlattices against PTO volume fraction. LDA, LSDA and WC calculations are compared to experimental data [1].

ferroelectric and paraelectric PTO differ. To approximate the average tetragonality of the structures we multiply the volume fractions of these materials with their lattice constant. To describe the amount of ferroelectric PTO in the material we introduce the order parameter α which is defined as

$$\alpha = \begin{cases} \frac{P}{P_{\text{bulk}}} & \text{ferroelectric regime} \\ 0 & \text{paraelectric regime} \end{cases}$$

where P stands for the polarization of the structure and P_{bulk} describes the polarization of bulk PTO. For the PTO volume fraction of 1 α thus becomes 1.

The tetragonality can then be computed using the following equation:

$$\begin{aligned} \frac{c}{a} &= \text{VF(SRO)} \cdot \left(\frac{c}{a}\right)_{\text{SRO}} + \text{VF(PTO)} \cdot \left(\alpha \left(\frac{c}{a}\right)_{\text{fePTO}} + (1-\alpha)\left(\frac{c}{a}\right)_{\text{pePTO}}\right) \\ &= (1 - \text{VF(PTO)}) \cdot \left(\frac{c}{a}\right)_{\text{SRO}} + \text{VF(PTO)} \cdot \left(\alpha \left(\frac{c}{a}\right)_{\text{fePTO}} + (1-\alpha)\left(\frac{c}{a}\right)_{\text{pePTO}}\right) \end{aligned}$$

where VF(structure) describes the volume fraction of the different structures.

LDA calculations were used to determine the parameters of the model. To compute the order parameter α we used a linear fit of the polarization in the ferroelectric regime.

Figure 6.5 shows that the model fits the experimental and LDA data quite nicely although the approximation has several shortcomings. We e.g. take the tetragonality of PTO which was calculated in a bulk PTO structure, i.e. in absence of an $\vec{E}$-field. However, in the superlattice structures the PTO unit cells are exposed to the depolarizing field which influences their tetragonality. Screening also changes the lattice constant of the metallic SRO unit cells.

6.2 Symmetric Structure with SrO-terminated SRO

6.2.1 Rumplings

We plot the layer rumplings for some sample symmetric structures with SrO-terminated SRO in figure 6.6 for the LDA approximation and in figure 6.7 for the WC GGA approximation.

As for the asymmetric superlattices, we notice that in PTO-rich structures the PTO layers are polarized as their rumplings are large and uniform, and SRO-rich structures are paraelectric with small rumplings. But there are two major differences. Firstly, the rumplings and therewith the polarization are smaller in these structures. Secondly, the onset of ferroelectricity is shifted to higher PTO volume fractions in the symmetric structures with SrO-terminated SRO layers. In the $(SRO)_1(PTO)_5$ superlattice the rumplings are already very small and the polarization almost vanishes.

Performing calculations with a WC exchange and correlation functional, the rumplings become again more pronounced, but in the $(SRO)_1(PTO)_5$ superlattice the rumplings become even smaller than in LDA calculations, implying once more that the ferroelectricity of the PTO layers is suppressed in this structure.

For structures with only one SRO unit cell we also performed spin polarized LDA calculations. The spin inclusion changes the rumplings in these structures only minimally, which agrees with the results found for the asymmetric superlattices.

In the symmetric structures the rumplings also change with the number of SRO unit cells as shown in figure 6.8. As for the asymmetric structures we observe that for ferroelectric structures the rumplings and the polarization decrease when increasing the number of SRO unit cells. Paraelectric structures remain paraelectric, independent of the number of metallic unit cells, and the rumplings of the PTO layers remain small.

6.2.2 Average Tetragonality

The average tetragonality of the symmetric superlattices with SrO-terminated SRO layers is plotted in figure 6.9. The shape of the curve is similar to the curve found for asymmetric structures, and we also see sudden changes in the average tetragonality if we compare structures with a similar PTO volume fraction but a different number of SRO unit cells. But the tetragonality of each structure is now smaller than before.

We also parametrized the model described above in 6.1.2 with parameters calculated from the symmetric superlattices, and find that it also fits the data quite well.

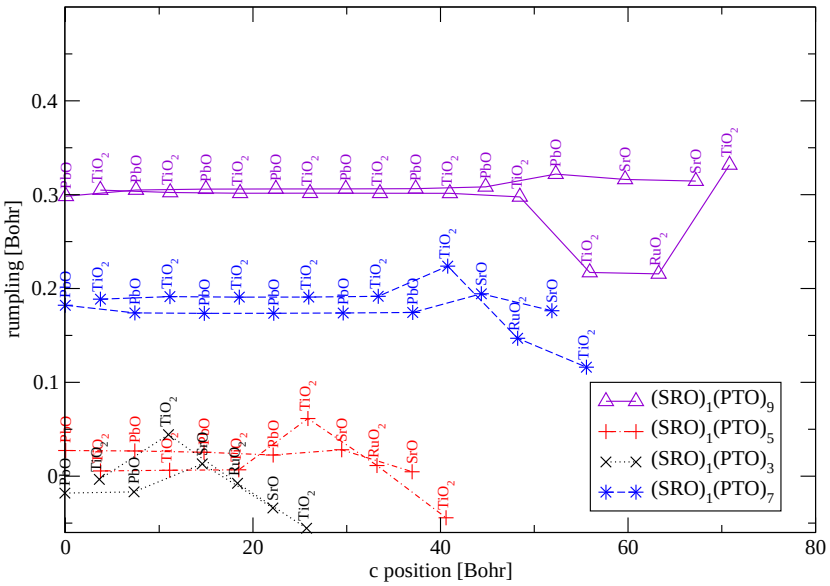

Figure 6.6: Layer rumpling for sample symmetric structures with SrO-terminated SRO layers. The atomic positions were relaxed using the LDA approximation.

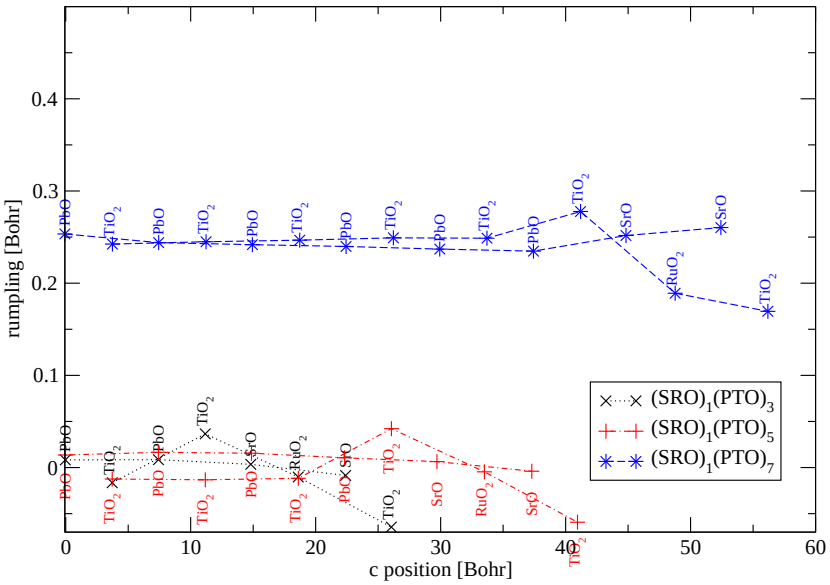

Figure 6.7: Layer rumpling for sample symmetric structures with SrO-terminated SRO layers. The atomic positions were relaxed using the WC calculation.

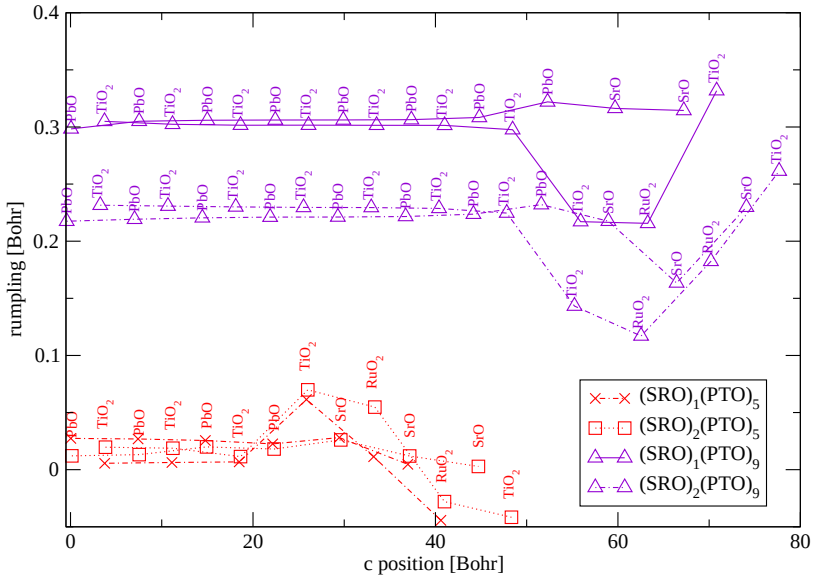

Figure 6.8: Comparison of layer rumplings for symmetric superlattices with SrO-terminated SRO layers. The structures contain the same number of PTO unit cells and 1 or 2 unit cells of SRO. LDA calculation.

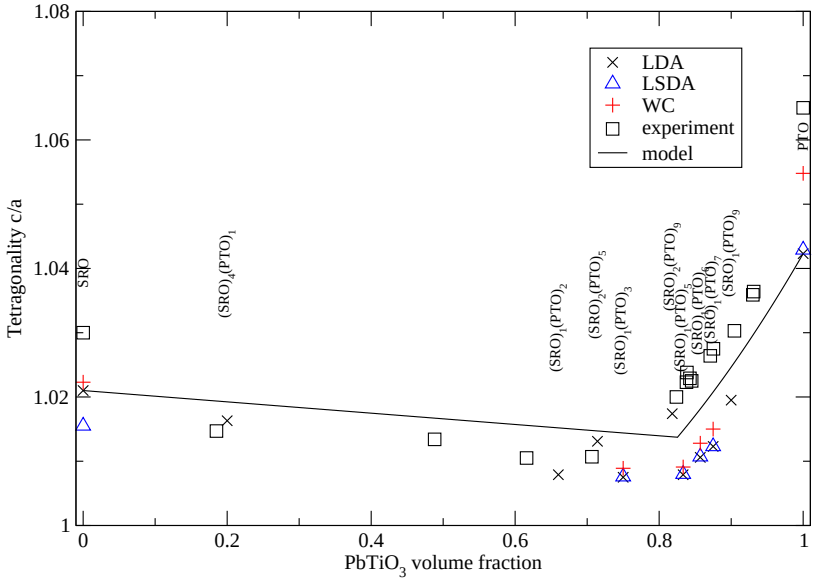

Figure 6.9: Average tetragonality $\frac{c}{a}$ versus PTO volume fraction. Experimental data [1], as well as results from LDA, LSDA and WC calculations are plotted. The results of the model explained in 6.1.2 are shown as well.

6.3 Symmetric Structure with RuO_2-terminated SRO

6.3.1 Rumplings

The layer rumplings of some sample symmetric structures with RuO_2-terminated SRO are shown in figure 6.10. In contrast to the layer rumplings seen in the other interface structures, we now find large, but very non-uniform, rumplings of the PTO unit cells even for high volume fractions of PTO. For low volume fractions the rumplings of the PTO unit cells become small, the PTO layers become paraelectric.

6.3.2 Average Tetragonality

The average tetragonality of symmetric structures with RuO_2-terminated SRO layers is shown in figure 6.11. The tetragonality $\frac{c}{a}$ of these symmetric structures is larger than the tetragonality found for the corresponding structures with the other interface structures. Especially for structures with a high PTO volume fraction the tetragonality seems to be very large compared to the experimental data [1], which would be uncharacteristic for LDA calculations which typically underestimate the lattice constants of ferroelectric structures.

As the structural properties don't really allow conclusions about the type of the interface, we tried to determine the experimental interface structure by X-ray diffraction which will be discussed in the next section.

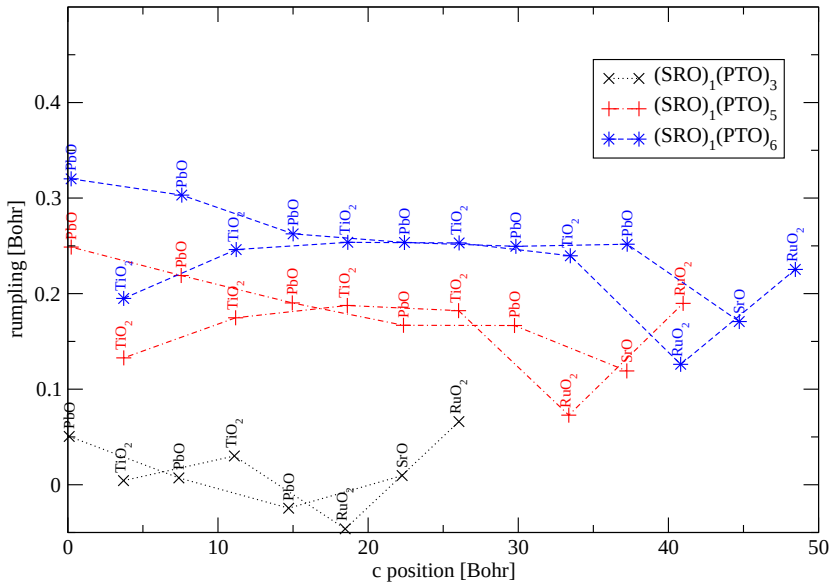

Figure 6.10: Layer rumplings for sample symmetric structures with RuO_2-terminated SRO layers. The atomic positions were relaxed using the LDA approximation.

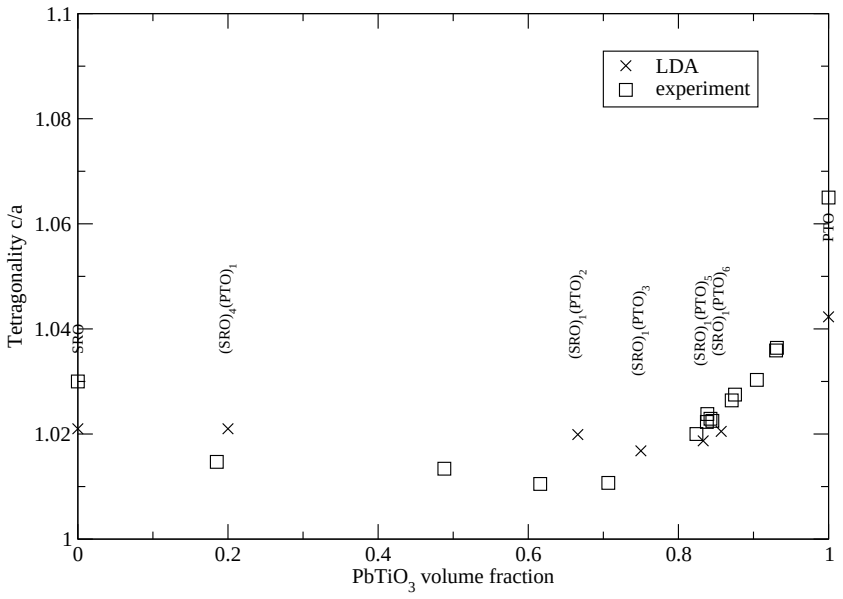

Figure 6.11: Average tetragonality $\frac{c}{a}$ of symmetric superlattices with RuO_2-terminated SRO layers. Experimental data [1] and results from a LDA calculation are depicted.

Chapter 7

X-ray Diffraction

7.1 Method

X-ray diffraction can be used to determine crystal structures. A beam of X-ray photons is scattered due to the electronic charge distribution in the material. The different position and form factors of the atoms affect the scattering and could make different interface structures distinguishable.

In the ideal kinematic regime, X-ray scattering can be thought of as the Fourier transform of the all-electron charge density. As density functional calculations determine the electronic charge density of the ground state, they seem to be helpful to analyze the experimental X-ray data. But in SIESTA [24] calculations, the core electrons are replaced by pseudopotentials, making the all-electron density not accessible. As the photons are mostly scattered by the core electrons, we approximate the scattering charge density by the charge density computed from the neutral atom potential.

To reproduce experimental data we compute the charge density of an artificial system modeling the experimental situation. As the main variations in the charge density between the different superlattice structures occur along the vertical c axis, experiments measured the X-ray scattering along this direction. When simulating the system, we can thus restrict the charge density to the charge density in c direction averaged over the x and y direction.

In c direction the charge density is composed of the charge density of the $SrTiO_3$ substrate chosen to have a thickness of a few μm. The charge density of the superlattice structure with 32 superlattice layers follows. The experimentalists grow superlattice films directly on top of the substrate, but to perform electrical experiments they sometimes also grow a thin electrode of about 32 layers on top of the substrate before they grow the superlattice structure. That's why a thin $SrRuO_3$ electrode can be optionally added to our artificial system. As the Fourier transform assumes a periodic repetition of the data given, the charge distribution ends in a thick vacuum layer.

The Fourier transform of the resulting charge density distribution was compared to the experimental X-ray data, which we discuss in the next section.

7.2 Results

As an example we compare the experimental X-ray measurements [1] of the $(SRO)_1(PTO)_5$ superlattice (see figure 7.1) to the theoretical calculations of the $(SRO)_1(PTO)_5$ superlattices (see figures 7.2, 7.3, 7.4) with

different interface structures (electrode is included in the calculations).

In experiment and theory we can attribute the peaks with the highest intensity to the substrate. Between two substrate peaks we find six peaks caused by the superlattice. The superlattice peaks are denoted by the order of the nearest substrate peak and their own order relative to the nearest substrate peak. The superlattice peak directly beside the substrate peak of first order is e.g. called the (001) peak, the superlattice peaks before and after are denoted as $(001) - 1$ and $(001) + 1$ peaks.

In the experimental data [1] we see that many peaks are split. Calculating the position of the superlattice peaks for a structure with a $(\mathrm{SRO})_1(\mathrm{PTO})_5$ and a $(\mathrm{SRO})_1(\mathrm{PTO})_6$ periodicity, we find that the splitting of the peaks is caused by the superposition of peaks from a $(\mathrm{SRO})_1(\mathrm{PTO})_5$ and a $(\mathrm{SRO})_1(\mathrm{PTO})_6$ superlattice.

In the following we only compare the peak intensities of the $(\mathrm{SRO})_1(\mathrm{PTO})_5$ superlattices. The positions of these peaks are marked in figure 7.1.

Comparing the simulations with the experimental measurements we notice that the order of magnitude between the superlattice peaks of different order deviate significantly in theory and experiment. These differences prohibit a direct comparison between theory and experiment. The only reasonable characteristics to compare are cancellations which should be consistent in theory and experiment.

In the X-ray curve of the asymmetric superlattice shown in figure 7.2, we do not see any cancellations. The other structures are more prone to cancellation as their structure is more symmetric. Indeed, we see a cancellation of the $(001) + 2$ and the $(003) - 2$ peak in the symmetric superlattice with a SrO-terminated SRO layer (see figure 7.3) . In the symmetric superlattice with a $\mathrm{RuO_2}$-terminated SRO layer we see a cancellation of the $(002) + 3$ peak and a partial cancellation of the $(003) + 2$ peak (see figure 7.4) .

Experimentally, we definitely see the $(001) + 2$ and the $(003) - 2$ peaks which should be canceled in the symmetric superlattice with a SrO-terminated SRO layer. Due to the experimental resolution in that area we can't tell if the $(002) + 3$ peak is canceled, but the $(003) + 2$ peak does not seem to be canceled.

Using the cancellations of peaks, we can conclude that the asymmetric interface structure seems like the most probable structure, but because of the large differences between theory and experiment, this result requires further confirmation.

In the next section we therefore compare the electrostatic properties of the different superlattice structures with the experiment.

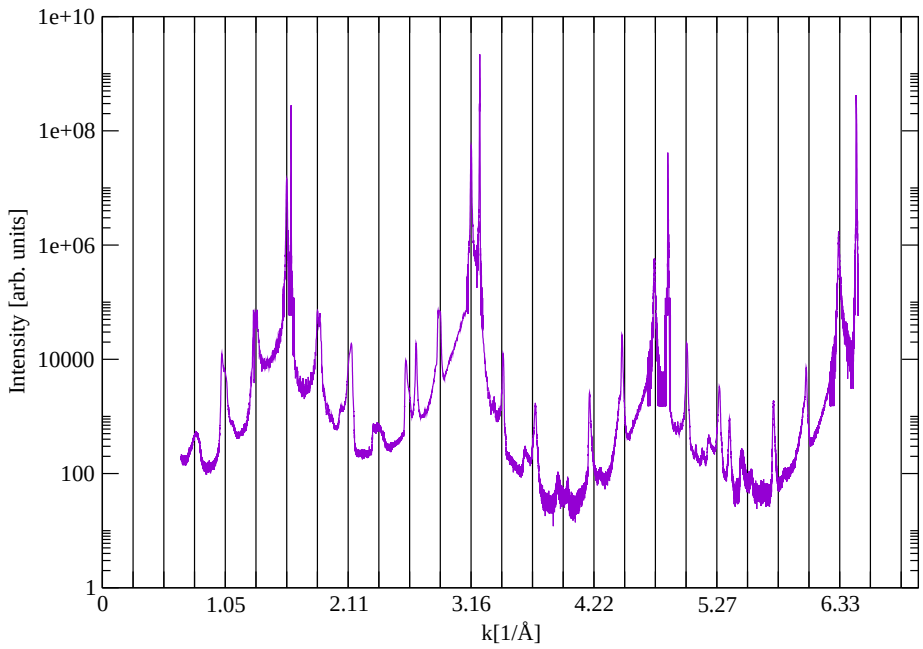

Figure 7.1: Experimental X-ray curve [1] of the $(SRO)_1(PTO)_5$ structure. The grid lines show the position of the equidistant peaks in the $(SRO)_1(PTO)_5$ superlattice

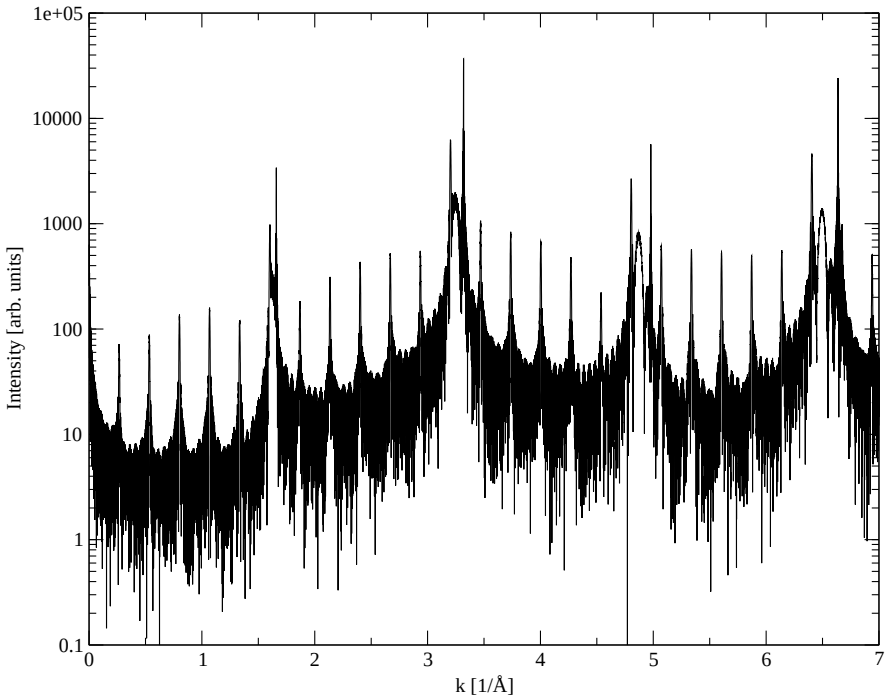

Figure 7.2: Theoretical X-ray curve of the asymmetric $(SRO)_1(PTO)_5$ structure

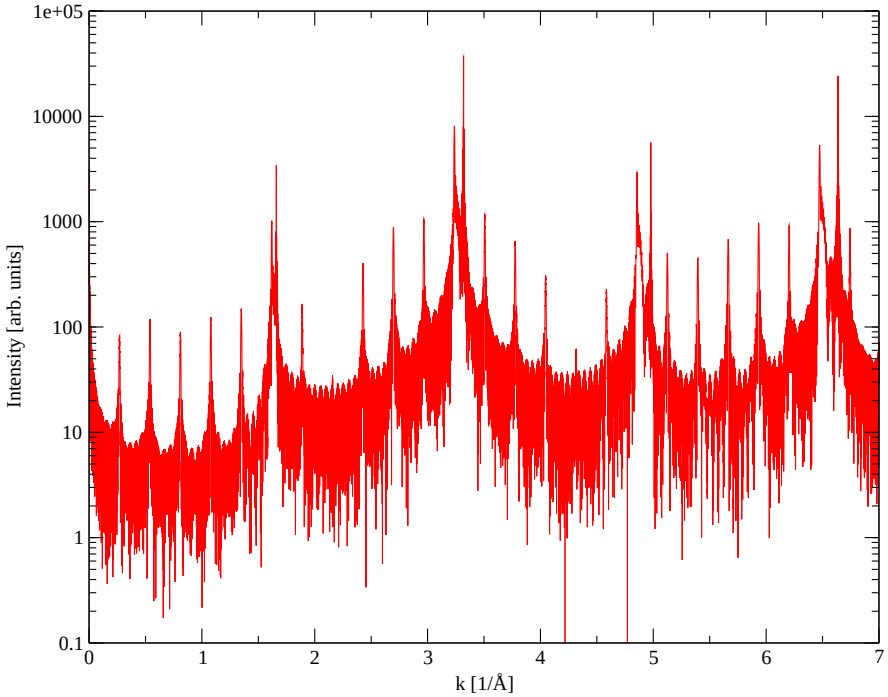

Figure 7.3: Theoretical X-ray curve of the symmetric $(SRO)_1(PTO)_5$ structure with SrO-terminated SRO layer

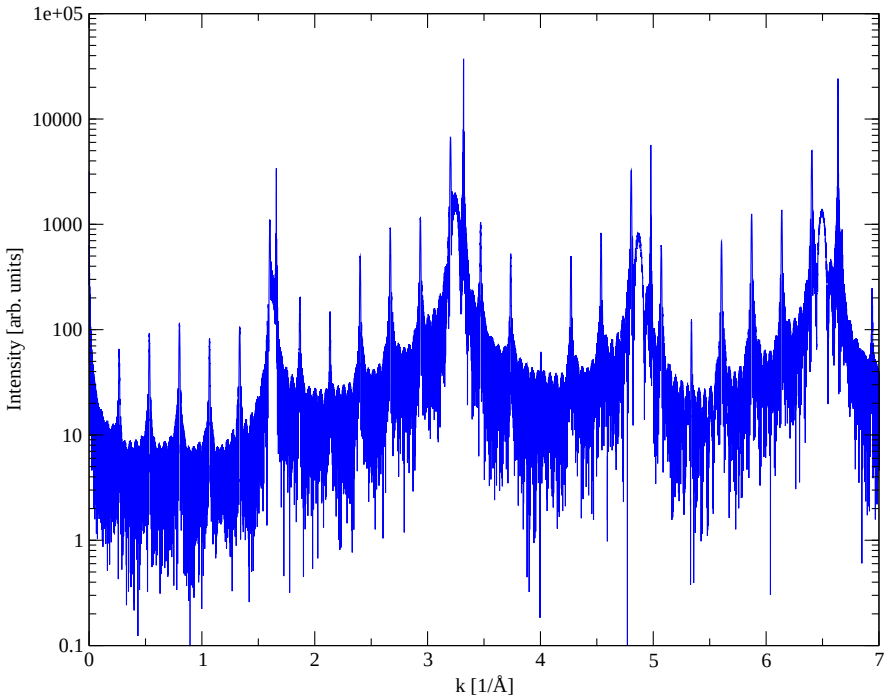

Figure 7.4: Theoretical X-ray curve of the symmetric $(SRO)_1(PTO)_5$ structure with RuO_2-terminated SRO layer

Chapter 8

Electrostatic Properties

In this section we take a look at the electrostatic properties of the different superlattices:

In Chapter 6 we saw that the PTO layers of structures with a high PTO volume fraction are ferroelectric. In this section we calculate and compare the layer polarization of these structures.

We also analyze the electrostatic potential of the superlattices:

The metallic SRO layers try to screen the charges at the surface of the ferroelectric layers but the screening is imperfect. Some of the surface charges can't be compensated by the metal and remain unscreened. This uncompensated charges create an electric field in the ferroelectric unit cells pointing against the polarization vector. Plotting the macroscopic average of the electrostatic field in the supercell (see figure for an example), we thus notice a uniform slope of the electrostatic potential caused by the electric field. The electric field is called depolarizing field as it destabilizes the polarization and can even lead to a break-down of the polarization if the field gets too strong.

8.1 Asymmetric Structure

The asymmetric structure has two different interfaces, which display different screening capabilities. A polarization pointing from the RuO_2 interface to the SrO interface (denoted as P_+) is screened differently from a polarization pointing from the SrO interface to the RuO_2 interface (denoted as P_-). This difference in screening causes differences in the layer rumplings and the polarization the system can sustain in the two polarization states. Figures 8.1 and 8.2 show the rumplings for some asymmetric structures in the P_- polarization state. The differences in the rumplings of the PTO layers show that the absolute value of the polarization changes, the differences in the rumplings of the SRO layers confirm that the polarization states P_+ and P_- are screened differently.

Figure 8.3 shows that the profile of the layer polarization[1] also differs for the two polarization states.

For both polarization states we find that the polarization increases for superlattices with a higher volume fraction of ferroelectric PTO unit cells. If the number of SRO unit cells is increased, the polarization

[1] We calculate the layer polarization by using the bulk Born effective charges as described in Section 2.3. Note that if we can identify a bulk structure in the PTO unit cells of the superlattice, we calculate the Born effective charges of a PTO unit cell in that bulk structure. If we can't identify a bulk structure (such as in $(SRO)_1(PTO)_3$, $(SRO)_2(PTO)_5$ or in the symmetric superlattices with RuO_2 terminated SRO layers), we approximate the Born effective charges by the Born effective charges of PTO constrained to a STO substrate. The calculation of the layer polarization becomes less accurate with this approximation as the reordering of electronic charges in the superlattice structure is not taken into account.

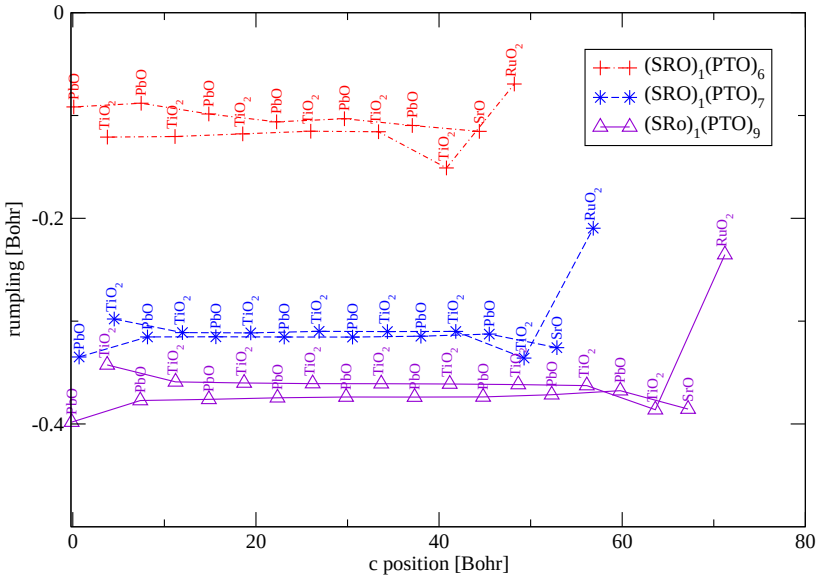

Figure 8.1: Rumplings of sample structures polarized in P_- direction. LDA calculation

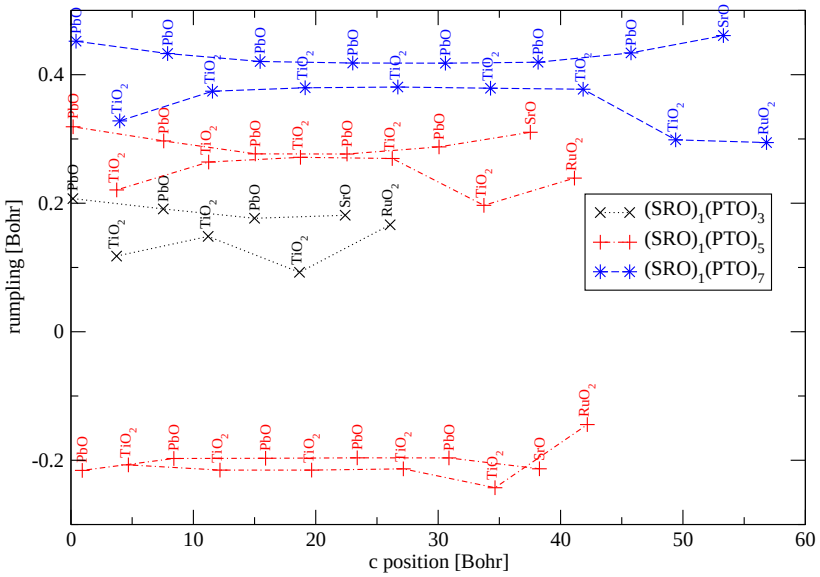

Figure 8.2: Rumplings of sample structures polarized in P_+ directions (positive rumplings) and in P_- direction (negative rumplings). The atomic positions were relaxed using the WC parametrization of the exchange and correlation functional.

decreases as the thicker metal layers now prohibit couplings between the ferroelectric layers, which enhance the ferroelectric polarization, more effectively.

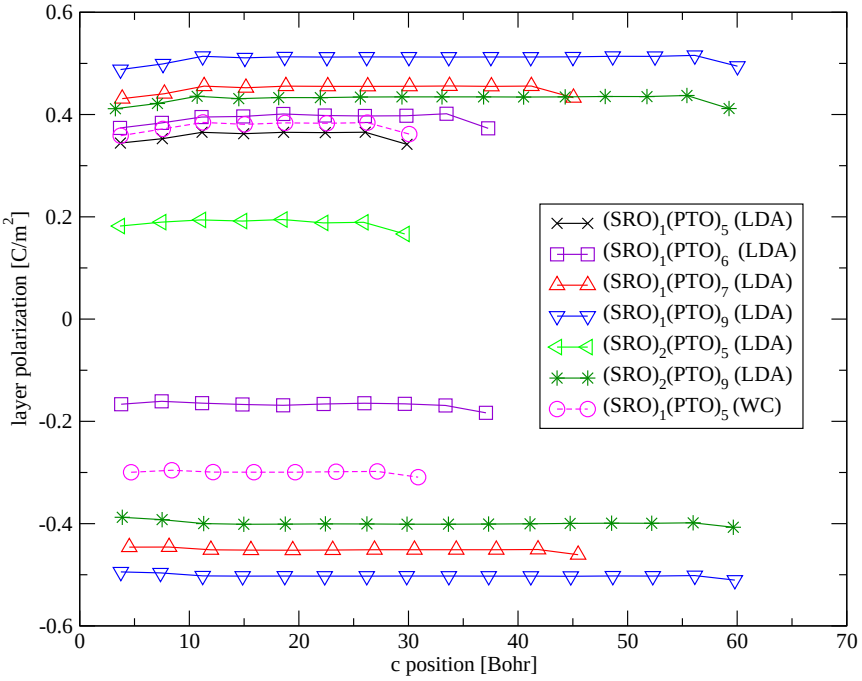

Figure 8.3: Layer polarization of sample asymmetric superlattices. The positive (negative) layer polarizations correspond to a $P_+(P_-)$ polarization. LDA and WC parametrization of the exchange and correlation functional were used. calculation

Structure	XC funct.	$\left(\frac{c}{a}\right)_{P_+}$	$\left(\frac{c}{a}\right)_{P_-}$	$P_+\left[\frac{\mathrm{C}}{\mathrm{m}^2}\right]$	$P_-\left[\frac{\mathrm{C}}{\mathrm{m}^2}\right]$	$(E_d)_{P_+}\left[\frac{\mathrm{eV}}{\mathrm{Bohr}}\right]$	$(E_d)_{P_-}\left[\frac{\mathrm{eV}}{\mathrm{Bohr}}\right]$
$(SRO)_1(PTO)_5$	LDA	1.0179	unstable	0.358	unstable	$-15.0\cdot10^{-3}$	unstable
$(SRO)_1(PTO)_6$	LDA	1.0173	1.0124	0.392	-0.168	$-16.1\cdot10^{-3}$	$+14.0\cdot10^{-3}$
$(SRO)_1(PTO)_7$	LDA	1.0208	1.0205	0.450	-0.451	$-15.0\cdot10^{-3}$	$+17.6\cdot10^{-3}$
$(SRO)_1(PTO)_9$	LDA	1.0232	1.0234	0.509	-0.502	$-14.1\cdot10^{-3}$	$+15.5\cdot10^{-3}$
$(SRO)_2(PTO)_5$	LDA	1.0160	unstable	0.187	unstable	$-12.1\cdot10^{-3}$	unstable
$(SRO)_2(PTO)_9$	LDA	1.0203	1.0197	0.431	-0.399	$-15.0\cdot10^{-3}$	$+16.3\cdot10^{-3}$
$(SRO)_1(PTO)_5$	WC	1.0160	1.0151	0.376	-0.300	$-15.0\cdot10^{-3}$	$+16.92\cdot10^{-3}$

Table 8.1: Comparison of tetragonality $\frac{c}{a}$, average layer polarization P and depolarizing field E_d of the two different polarization states P_+ and P_-.

In table 8.1 we compare the two polarization states of the different structures to each other. For structures with a high PTO volume fraction, the differences in the average tetragonality, in the rumplings and in the average layer polarization, are small. For structures with few PTO unit cells the differences are large. Using LDA calculations we find that structures with 5 or less PTO unit cells have only one stable, polar state (the P_+ state). When the relaxation calculation is started from an initial configuration corresponding to the P_- polarization state, the atoms move back to the P_+ polarization state. The authors of [23] proposed such a

self-poling behavior in three-component superlattices caused by a compositional breaking of the inversion symmetry. We already find a self-poling behavior in the two-component SRO/PTO superlattices in which the inversion symmetry is broken by the asymmetric interface structure.

To get a better understanding of these structures, we calculate the total energy of the system for atomic displacements along the line $\vec{r} = \vec{r}_{P_+} + u \cdot \left(\vec{r}_{P_-} - \vec{r}_{P_+}\right)$ interpolating linearly between the minima P_+ and P_- of the energy. Figures 8.4 and 8.5 show the calculated double-well potential for LDA and WC calculations. To compare structures with a different composition, we do not plot the total energy but the energy per unit cell. The differences in energy per unit cell between the two polarization states and the saddle point of the energy curve are given in table 8.2. The table also shows the corresponding differences in energy for bulk PTO constrained to a STO substrate.

Table 8.2 shows that the difference in energy between the polarization states decreases if the PTO volume fraction increases. We can understand this behavior remembering that in the limit of infinite PTO layers between the metallic layers, i.e. the PTO bulk structure, the difference in energy between the two polarization states has to vanish. The difference in energy between the saddle point and the P_- polarization state decreases moving away from the infinite PTO system. For the $(\mathrm{SRO})_1(\mathrm{PTO})_6$ structure, the double-well potential is almost non-existent in LDA calculations. For the $(\mathrm{SRO})_1(\mathrm{PTO})_5$ structure, we then only find one stable, polar state. The $(\mathrm{SRO})_1(\mathrm{PTO})_3$ superlattice also has solely one stable state.

Using WC calculations we observe that the $(\mathrm{SRO})_1(\mathrm{PTO})_5$ has two stable states. Table 8.2 shows that the double-well of PTO is higher in WC calculations than in LDA calculations. Thus the P_- state of the $(\mathrm{SRO})_1(\mathrm{PTO})_5$ structure is still stable in WC calculations, unlike in LDA calculations.

Table 8.1 shows why the polarization can switch from the P_- to the P_+ polarization state. Comparing the depolarizing field of the structure in the two polarization states, we see that the depolarizing field is always stronger in the P_- polarization state, indicating that the screening of the P_- polarization is worse. In structures with few PTO unit cells the double-well of the potential is low and the electric field is strong enough to overcome the double-well and depolarize the P_- state, switching it to the P_+ polarization state. For high PTO volume fractions the double-well potential is more pronounced as there is more coupling between the ferroelectric layers and the polarization is larger. In these materials the P_+ and the P_- polarization are thus stable.

Only for the $(SRO)_1(PTO)_6$ structure we find that the depolarizing field is smaller for the P_- than for the P_+ polarization state. But in this structure the asymmetry in the potential (see figure 8.4) already causes the P_- polarization to drop considerably, creating the small depolarizing field.

Structure	XC functional	$\frac{E_{P_+}-E_{P_-}}{n}$ [meV]	$\frac{E_{P_+}-E_S}{n}$ [meV]	$\frac{E_{P_-}-E_S}{n}$ [meV]
$(\mathrm{SRO})_1(\mathrm{PTO})_6$	LDA	-11.9	-12.0	-0.2
$(\mathrm{SRO})_1(\mathrm{PTO})_7$	LDA	-10.0	-21.9	-11.9
$(\mathrm{SRO})_1(\mathrm{PTO})_9$	LDA	-8.8	-30.9	-22.1
$(\mathrm{SRO})_2(\mathrm{PTO})_9$	LDA	-7.1	-17.0	-9.9
PTO	LDA	0	-125	-125
$(\mathrm{SRO})_1(\mathrm{PTO})_5$	WC	-11.7	-16.4	-4.7
PTO	WC	0	-187	-187

Table 8.2: Difference in total energy $\frac{E_{P_+}-E_{P_-}}{n}$ per unit cell between the two minima of the double-well potential, energy difference $\frac{E_{P_{+/-}}-E_S}{n}$ per unit cell between the saddle point S and the P_+ /P_- polarization state.

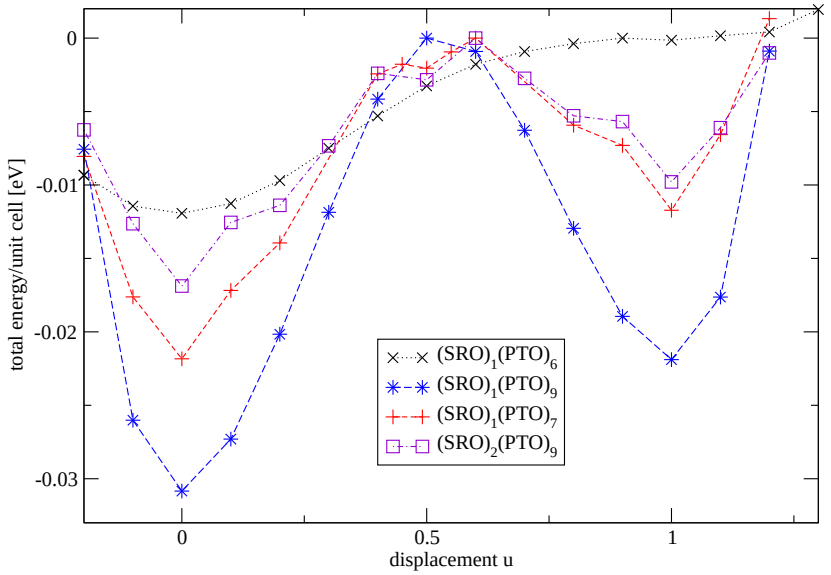

Figure 8.4: Total energy per unit cell versus displacement along the line $\vec{r} = \vec{r}_{P_+} + u \cdot \left(\vec{r}_{P_-} - \vec{r}_{P_+}\right)$which connects the polarization states P_+ and P_- of asymmetric superlattices. LDA calculation

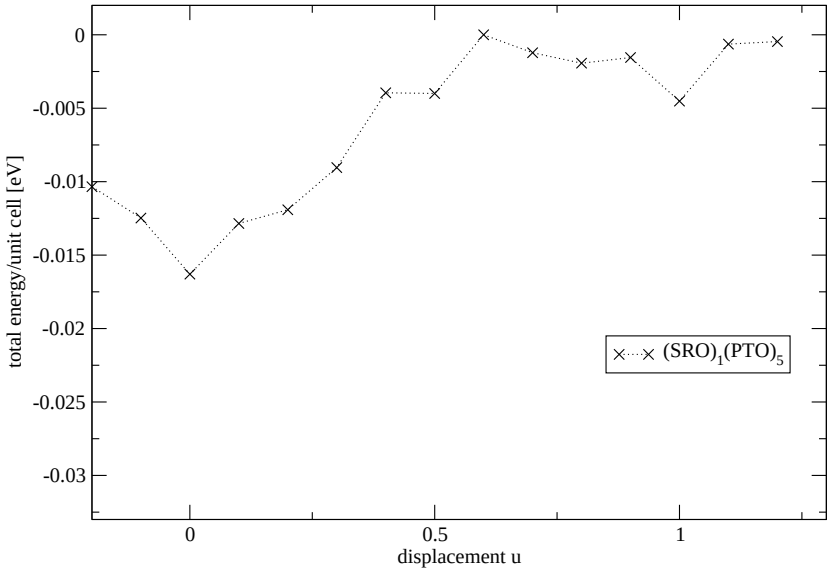

Figure 8.5: Total energy per unit cell versus displacement along the line which connects the $\vec{r} = \vec{r}_{P_+} + u \cdot \left(\vec{r}_{P_-} - \vec{r}_{P_+}\right)$which connects the polarization states P_+ and P_- of the $(\mathrm{SRO})_1(\mathrm{PTO})_5$ superlattice. WC calculation

To compare the theoretically calculated polarization with the experimentally measured polarization, we compute the difference between the average polarization P_+ and P_- , halved this difference, and multiplied by the PTO volume fraction, as only the PTO layers are ferroelectric and contribute to the polarization. The experimental [1] and theoretical data are shown in figure 8.6.

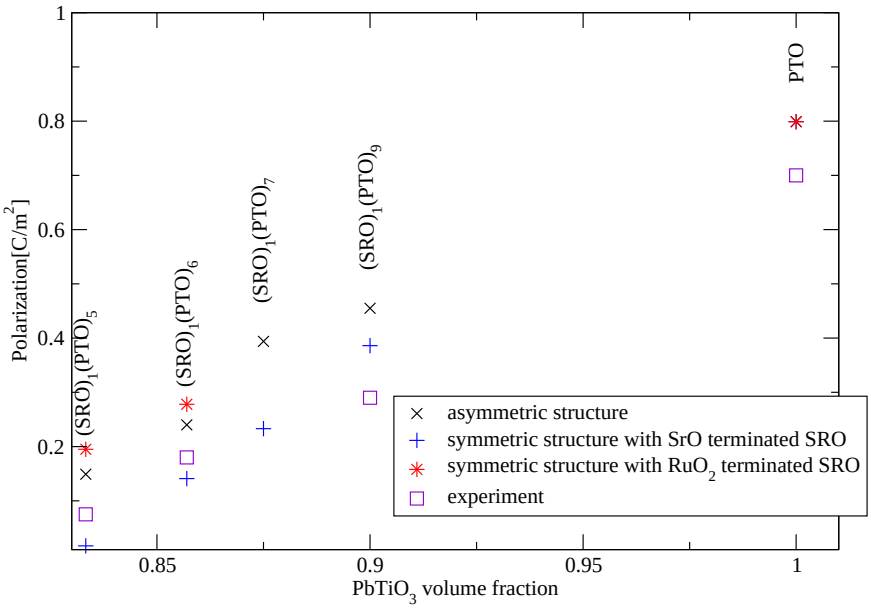

Figure 8.6: Bulk polarization of the structures with different interfaces. LDA calculations are compared with experimental values [1]

Comparing the PTO bulk polarizations we notice the typical overestimation of the polarization in DFT calculations. But even considering this overestimation, the calculated polarizations seem too high compared to the experimental values, especially for structures with few PTO unit cells. An experimental fact that agrees with the theoretically observed polar states is that in the $(SRO)_1(PTO)_5$ sample, there are no ferroelectric domains anymore visible [1].

There are even more asymmetries in the system. For structures with less than five PTO unit cells it is not possible to determine the field strength of the depolarizing field, as there is no bulk structure anymore, and taking the macroscopic average of the electrostatic potential yields a non uniform slope of the potential. But comparing the electrostatic potential of the $(SRO)_1(PTO)_5$ (cf. figure 8.7)to the electrostatic potential of the $(SRO)_1(PTO)_3$ structure (cf. figure 8.8), we nevertheless see that the depolarizing field changes its direction, although the rumplings (and therewith also the polarization) of the $(SRO)_1(PTO_3$ structure still have the same form and shape as in the $(SRO_1(PTO)_5$ superlattice.

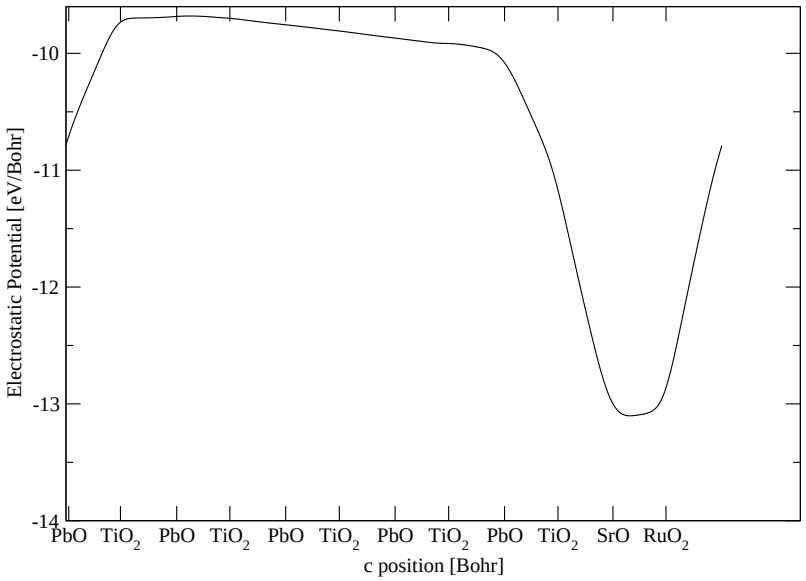

Figure 8.7: Electrostatic potential of asymmetric $(SRO)_1(PTO)_5$ structure. LDA calculation

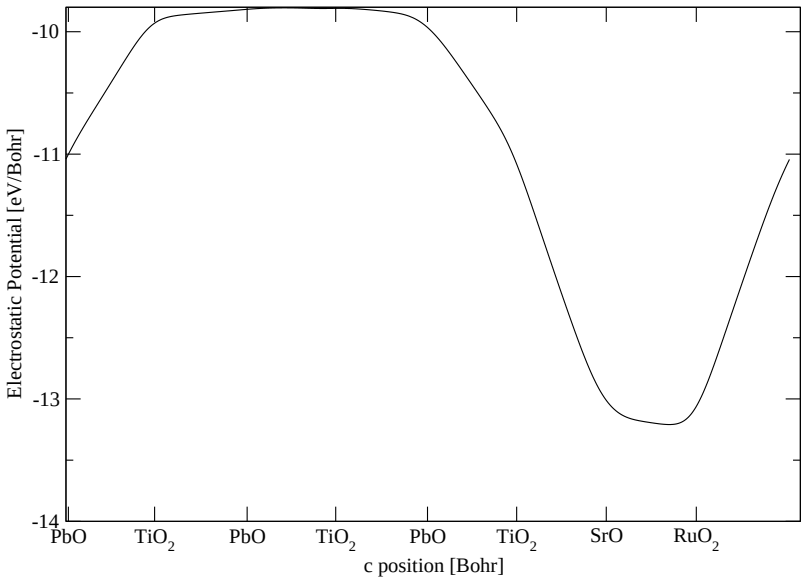

Figure 8.8: Electrostatic potential of asymmetric $(SRO)_1(PTO)_3$ structure. LDA calculation

Structure	$E_d \left[\frac{\text{eV}}{\text{Bohr}}\right]$	$P\left[\frac{\text{C}}{\text{m}^2}\right]$
$(\text{SRO})_1(\text{PTO})_5$	$1.7 \cdot 10^{-3}$	0.020
$(\text{SRO})_1(\text{PTO})_6$	$8.9 \cdot 10^{-3}$	0.164
$(\text{SRO})_1(\text{PTO})_7$	$13.5 \cdot 10^{-3}$	0.272
$(\text{SRO})_1(\text{PTO})_9$	$17.5 \cdot 10^{-3}$	0.429
$(\text{SRO})_2(\text{PTO})_5$	$4.7 \cdot 10^{-3}$	0.021
$(\text{SRO})_2(\text{PTO})_9$	$16.3 \cdot 10^{-3}$	0.328

Table 8.3: Depolarizing field E_d and average layer polarization P for symmetric superlattices with SrO terminated SRO layers

8.2 Symmetric Structure with SrO-terminated SRO

The layer polarization of symmetric structures with SrO-terminated SRO layers is depicted in figure 8.9. Away from the interfaces the layer polarization takes a uniform value. Only at the interface layers the rumplings cause deviations in the layer polarization profile. The shape of the layer polarization looks different from the shape of the layer polarization in the asymmetric interfaces, as only one interface of the symmetric superlattice matches the interfaces in the asymmetric structure, resulting in a similar polarization profile at that interface. The composition of the other interface differs causing different rumplings and layer polarizations.

As already seen above for the asymmetric superlattices, we find that the layer polarization decreases as there are less ferroelectric PTO unit cells, but a constant number of SRO unit cells in the structure. When the number of SRO unit cells is increased and the number of PTO unit cells is kept constant, the polarization decreases as well, because the metal unit cells constrict the couplings between the ferroelectric layers which enhances the polarization.

The depolarizing field changes with the polarization. When the polarization increases but the number of screening SRO unit cells remains constant, the depolarizing field increases as well as more charges remain unscreened.

In figure 8.6 we compare the polarization for this symmetric superlattice with experiment. We find that the ferroelectricity sets in later for the symmetric superlattices with SrO-terminated SRO layers. The $(\text{SRO})_1(\text{PTO})_5$ superlattice is still ferroelectric in experiments, whereas the $(\text{SRO})_1(\text{PTO})_5$ superlattice barely displays any PTO rumplings or polarization in the ab initio calculations.

8.3 Symmetric Structure with RuO_2-terminated SRO

We also calculated the layer polarization and the depolarizing field for the symmetric superlattice with a RuO_2 termination of the SRO layers (see figure 8.10 and table 8.4). The profile of the layer polarization mirrors that the layer rumplings are very non-uniform, even far away from the interfacial layers (see figure 6.10).

Structure	$E_d \left[\frac{\text{eV}}{\text{Bohr}}\right]$	$P\left[\frac{\text{C}}{\text{m}^2}\right]$
$(\text{SRO})_1(\text{PTO})_5$	$16.6 \cdot 10^{-3}$	0.233
$(\text{SRO})_1(\text{PTO})_6$	$17.7 \cdot 10^{-3}$	0.325

Table 8.4: Depolarizing field E_d and layer polarization P of symmetric superlattices with RuO_2-terminated SRO

Figure 8.6 shows the polarization of the symmetric structure with RuO_2-terminated SRO compared to experimentally measured polarizations and the polarizations of the other two interface structures. One notices that the polarization for the symmetric superlattices with RuO_2-terminated SRO is even higher than the polarization of the asymmetric superlattices, which already overestimated the experimental values by far, as discussed above.

Considering the deviations in polarization and in the structural properties and the energetics it seems unlikely that the experimentally realized interface structure is symmetric with RuO_2-terminated SRO layers.

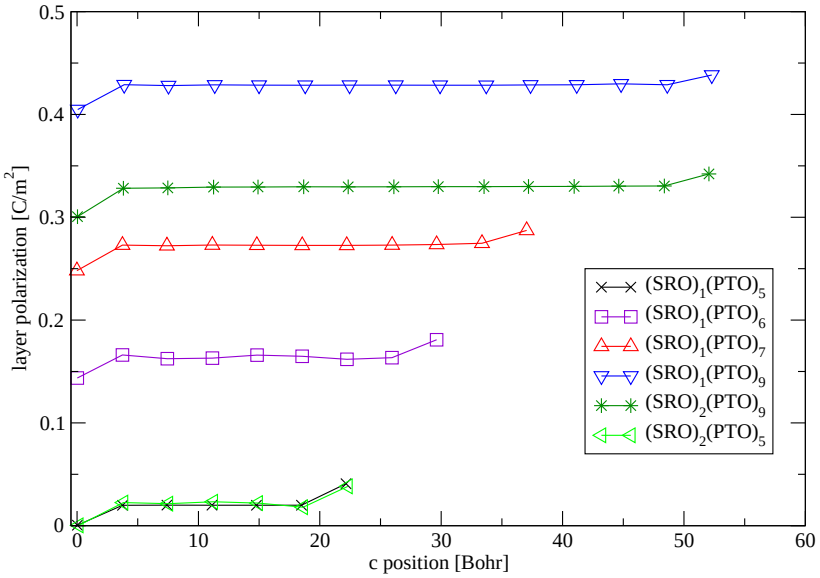

Figure 8.9: Layer polarization P of different symmetric superlattices with SrO-terminated SRO layers

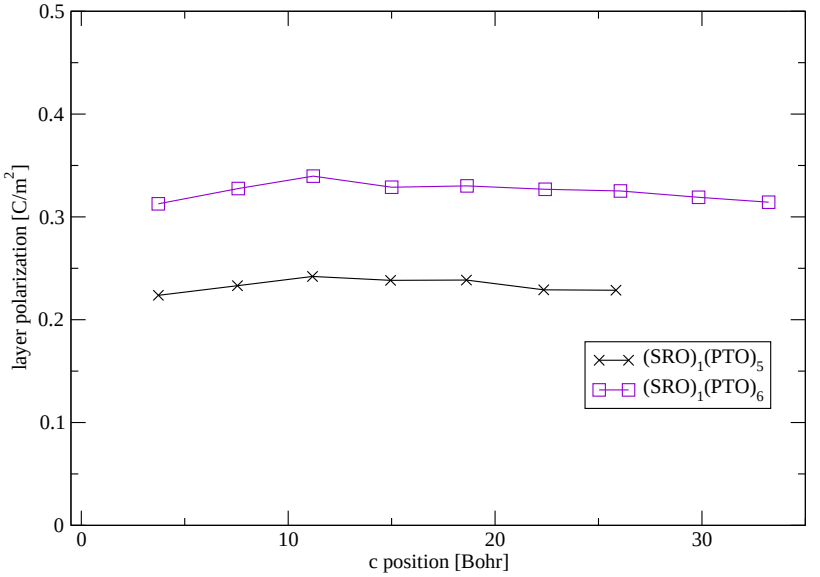

Figure 8.10: Layer polarization P of different symmetric superlattices with RuO_2-terminated SRO layers

Chapter 9

Electronic Properties

In the following section we analyze the band structure and the density of states of the different superlattices.

9.1 Asymmetric Superlattices

Figure 9.1 shows the band structure of asymmetric $(SRO)_1(PTO)_5$ which was calculated using the LDA approximation. One notices that there are single bands near the Fermi energy E_f belonging to the single SRO unit cell of the superlattice. Most of the other bands are fivefold degenerate and can thus be attributed to the PTO unit cells. We can conclude that the SRO layer of the structure is metallic and most of the PTO layers remain insulating.

Calculations of the projected density of states as shown in figure 9.2 confirm this conclusion. The density of states at the Fermi level is non-zero in the metallic layer and in one PTO layer. In the unit cells of the PTO bulk, conduction and valence band are separated by an energy gap.

To reproduce experimental band gaps we also performed band structure calculations including additional Hubbard U terms. In these calculations the structures were still relaxed using spin-polarized LDA calculations, but after the relaxation additional Hubbard U terms were used in the calculation of the band structure. The Hubbard terms were included on the very localized Ru 4d orbital and Ti 3d orbital. The Hubbard $U_{\mathrm{Ru,4d}}$ term we used was fitted by [27] to describe STO/SRO superlattices optimally. The Hubbard $U_{\mathrm{Ti,3d}}$ term was optimized by [17] for the calculation of rutile TiO_2 .

As can be seen in figure $(SRO)_1(PTO)_5$ becomes almost half metallic in these calculations, as the Fermi energy only barely cuts one of the spin bands.

The band structure for other structures containing one SRO unit cell looks similar to the band structures shown above. But depending on the number of PTO unit cells, the magnitude of the direct bandgap changes as shown in figure 9.4. This change in the bandgap is an effect of confinement. The ferroelectric layers are confined in c direction by the metallic SRO layers. Reducing the number of PTO unit cells increases the confinement in the vertical direction resulting in a larger bandgap and vice versa.

9.2 Symmetric Structure with SrO-terminated SRO

Figure 9.5 shows the band structure of symmetric $(SRO)_1(PTO)_5$ with a SrO-terminated SRO layer. The band structure was calculated using the local density approximation.

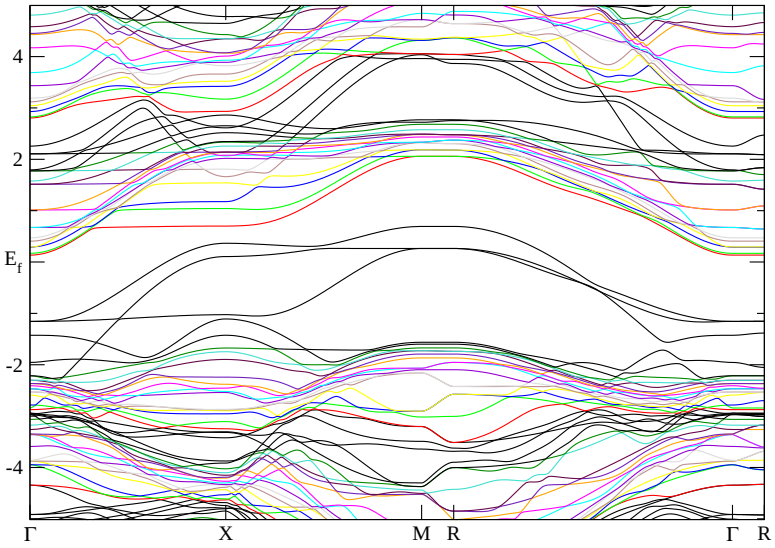

Figure 9.1: Band structure of asymmetric $(SRO)_1(PTO)_5$. LDA calculation

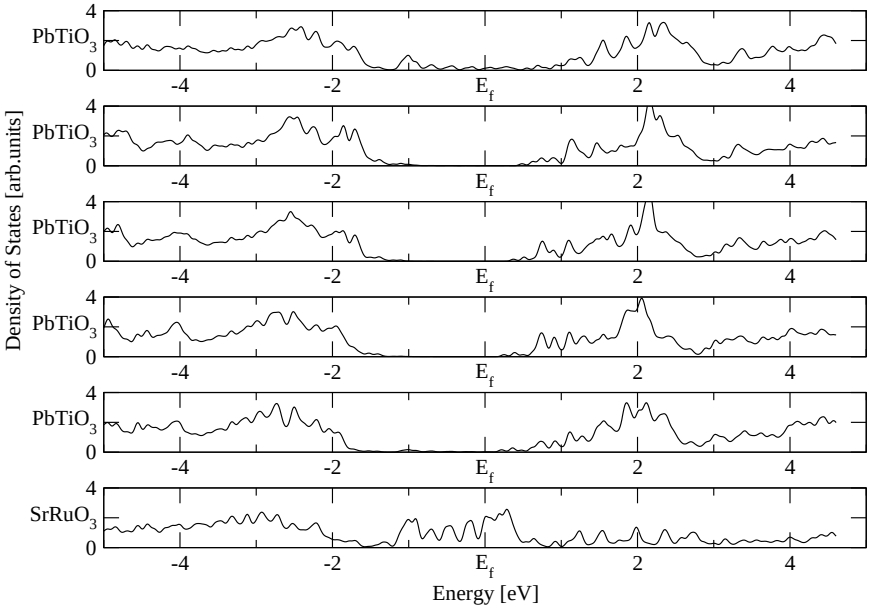

Figure 9.2: Layer-by-layer projected density of states of the asymmetric $(SRO)_1(PTO)_5$ superlattice

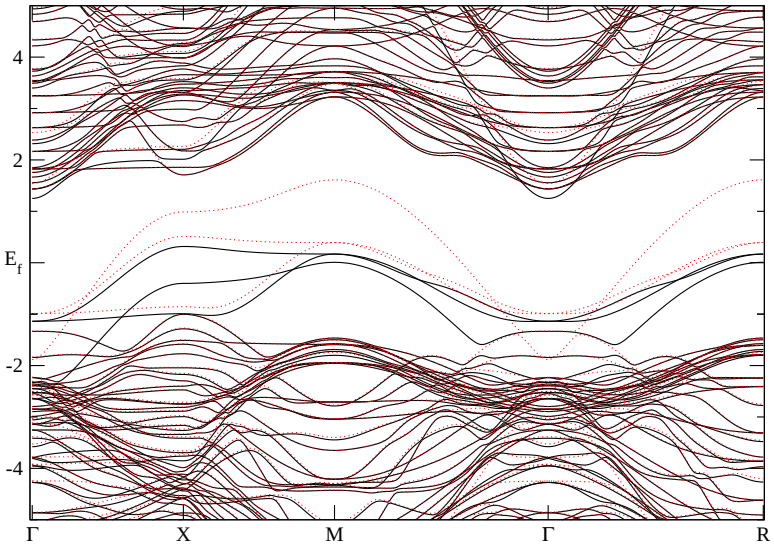

Figure 9.3: Band structure of asymmetric $(\mathrm{SRO})_1(\mathrm{PTO})_5$. The atomic positions were relaxed in a LSDA calculation. Additional Hubbard terms were included to calculate the band structure ($U_{\mathrm{Ru,4d}} = 4.0\mathrm{eV}$, $U_{\mathrm{Ti,3d}} = 9.4\mathrm{eV}$). The dotted and the straight lines show the band lines for the different spins.

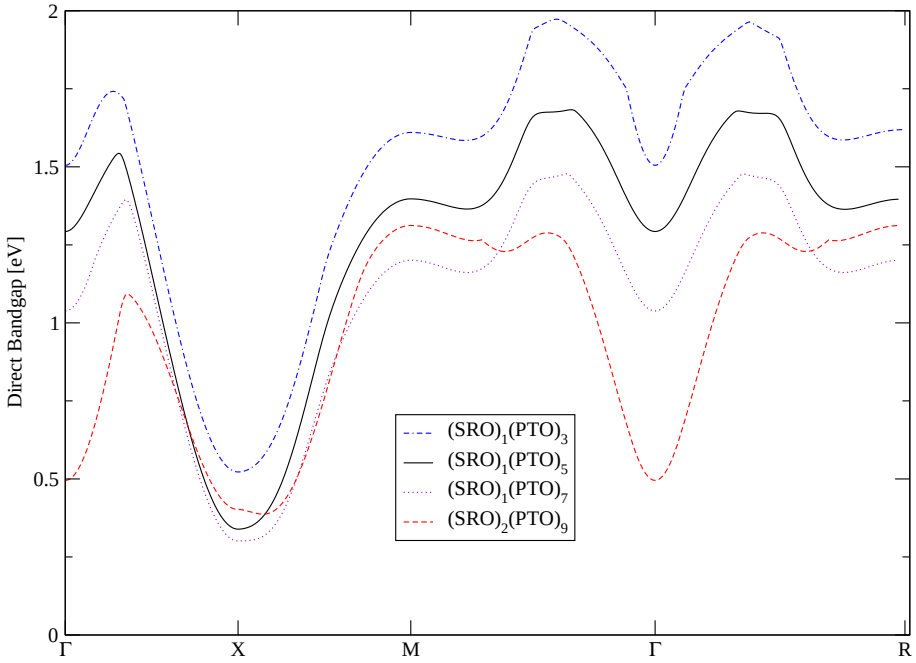

Figure 9.4: Direct bandgap of different SRO/PTO superlattices. LDA calculation

Comparing this band structure to the band structure of asymmetric $(SRO)_1(PTO)_5$ shown in figure 9.1, we see that the band structures look very similar.

The layer-by-layer projected density of states depicted in figure 9.6 also looks quite similar. The SRO layer is metallic as well as the STO layer, whereas the bulk PTO layers are insulating.

Computing the direct bandgap for structures with different numbers of PTO unit cells, we also see a confinement effect which is similar to the confinement effect for asymmetric superlattices.

9.3 Symmetric Structure with RuO_2-terminated SRO

The band structure of symmetric $(SRO)_1(PTO)_5$ with a RuO_2-terminated SRO layer is shown in figure 9.7. The calculations for this band structure were performed using the local density approximation.

Comparing the band structure of figure 9.7 to the band structure of the $(SRO)_1(PTO)_5$with the other interface structures (see figure 9.1 and 9.5) we notice a main difference. We now find no single, but doubly degenerate bands near the Fermi energy E_f . The other band lines resemble the bands found in the other structures. This finding implies that the bands near the Fermi energy are bands of Ru character as the difference in composition between the symmetric structure with RuO_2-terminated SRO bands and the other two interface structures is the number of Ru atoms. We can furthermore conclude that the metallic character of these structures is more pronounced as there are more bands crossing the Fermi level.

The plot of the layer-by-layer projected density of states shown in figure 9.8 confirms this finding. Now the SRO and the PRO layer have a distinctly metallic character and one PTO layer is also metallic.

In the next section we analyze the spin polarization of the different structures. As we found in the chapters before that the symmetric interface with RuO_2-terminated SRO layers seems like the most improbable interface structure, we concentrate on the asymmetric and symmetric structures with SrO-terminated SRO layers from now on.

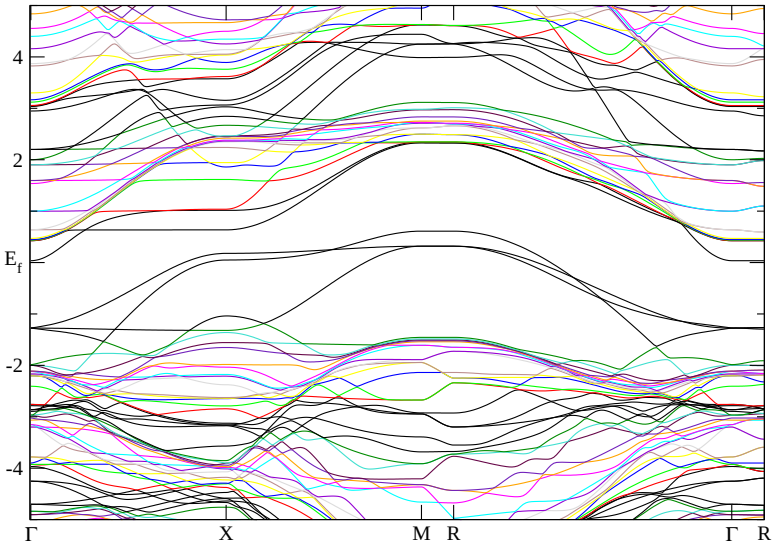

Figure 9.5: Band structure of symmetric $(SRO)_1(PTO)_5$ with a SrO-terminated SRO layer. LDA calculation

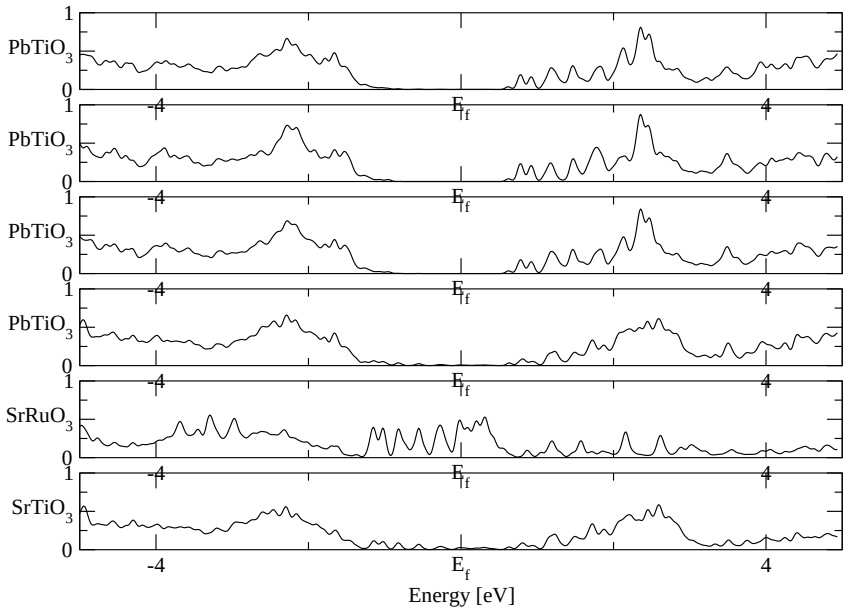

Figure 9.6: Layer-by-layer projected density of states of the symmetric $(SRO)_1(PTO)_5$ superlattice with a SrO-terminated SRO layer

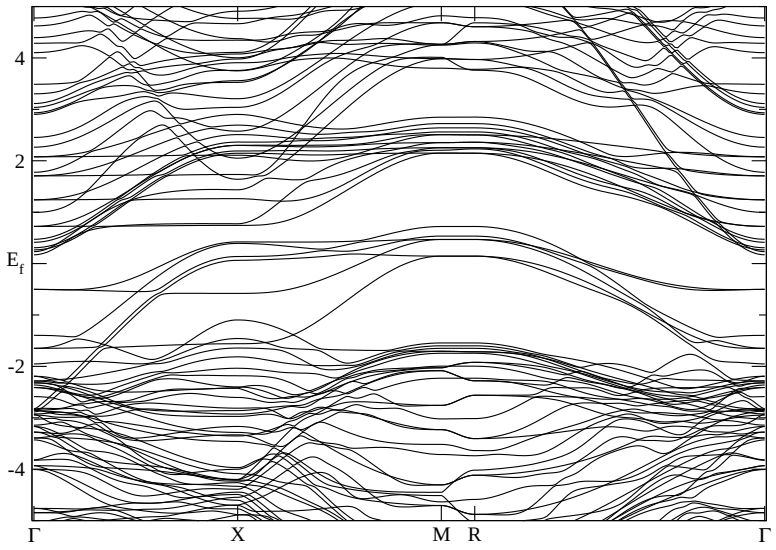

Figure 9.7: Band structure of symmetric $(SRO)_1(PTO)_5$ superlattices with a RuO_2-terminated SRO layer. LDA calculation

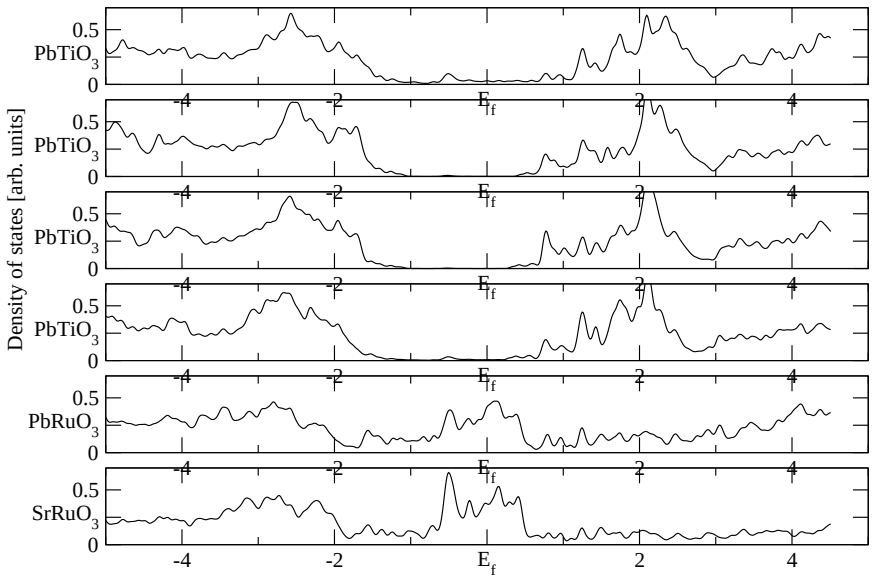

Figure 9.8: Layer-by-layer projected density of states of the symmetric $(SRO)_1(PTO)_5$ superlattice with a RuO_2-terminated SRO layer

Chapter 10

Spin Polarization

10.1 Asymmetric Structure

Including the spin in the LDA calculations, we find that the spin polarization of all the asymmetric structures containing one SRO unit cell has the same value (see table 10.1). When more SRO unit cells are added, the spin polarization changes.

Interestingly, the spin polarization of $(SRO)_1(PTO)_7$ does not differ for the polarization states P_+ and P_- but for the $(SRO)_2(PTO)_9$ superlattice the spin polarization of the P_+ state is different from the spin polarization of the P_- state. In $(SRO)_2(PTO)_9$ there is a weak coupling between the polarization and the spin polarization, whereas these two properties do not seem to be coupled in the asymmetric structures containing only one SRO unit cell.

Structure	spin polarization(P_+)[e]	spin polarization(P_-)[e]
$(SRO)_1(PTO)_3$	0.44	-
$(SRO)_1(PTO)_5$	0.44	-
$(SRO)_1(PTO)_7$	0.44	0.44
$(SRO)_2(PTO)_9$	1.77	1.55
$(SRO)_4(PTO)_1$	3.98	-

Table 10.1: Spin polarization of asymmetric superlattices for the two different polarization states. LSDA calculation

10.2 Symmetric Structure with SrO-terminated SRO

For the symmetric structures with SrO-terminated SRO we also performed spin-polarized LDA calculations. Table 10.2 shows that the spin polarization does not differ for the structures analyzed. Comparing the spin polarization of these symmetric superlattices with the spin polarization of the asymmetric superlattices (cf. table 10.1) we see that the spin polarization of the symmetric structures with one SRO unit cell equals even the spin polarization of the asymmetric structure containing one SRO unit cell. This implies that the spin polarization depends on the number of RuO_2 layers.

It would be interesting to calculate the spin polarization of symmetric structures with more than one RuO_2 layer as we find different spin polarizations of the two different polarization states in the corresponding

asymmetric structures.

Structure	Spin polarization [e]
$(SRO)_1(PTO)_3$	0.44
$(SRO)_1(PTO)_5$	0.44
$(SRO)_1(PTO)_6$	0.44
$(SRO)_1(PTO)_7$	0.44

Table 10.2: Spin polarization of symmetric superlattices with SrO-terminated SRO layers

Chapter 11

Effect of Strain

Ferroelectrics are known to be very sensitive to the applied misfit strain [21], i.e. the constrained in-plane lattice constant a. In the next section we thus analyze the strain dependence of the properties discussed above.

11.1 Formation Energy

First, we analyze how the difference in formation energy changes under different strain conditions.

In table 11.1 and in table 11.2 we compare the formation energy between an asymmetric superlattice and a symmetric superlattice with SrO-terminated SRO layers for a LDA calculation and a WC calculation respectively. For both parametrizations of the exchange and correlation functional the most stable structure remains the same independent of the strain. But we find that compressing the in-plane lattice constant a decreases the difference in formation energy, i.e. the asymmetric structure becomes less favored. In contrast, stretching the in-plane lattice constant a increases the difference in formation energy, making the asymmetric structure more favored.

Structure	$\Delta E_{\text{formation}}$[eV] $a = 3.82$Å	$\Delta E_{\text{formation}}$[eV] $a = 3.87$Å	$\Delta E_{\text{formation}}$[eV] $a = 3.92$Å
$(\text{SRO})_1(\text{PTO})_3$	-0.048	-0.014	-0.001
$(\text{SRO})_1(\text{PTO})_5$	+0.009	+0.009	+0.012

Table 11.1: Formation energy of symmetric superlattices with SrO-terminated SRO layers compared to formation energy of corresponding asymmetric superlattices for different misfit strains. The relaxation calculations were done using the local density approximation.

Structure	$\Delta E_{\text{formation}}$[eV] $a = 3.87$Å	$\Delta E_{\text{formation}}$[eV] $a = 3.905$Å
$(\text{SRO})_1(\text{PTO})_3$	-0.056	-0.039
$(\text{SRO})_1(\text{PTO})_5$	+0.009	+0.006

Table 11.2: Formation energy of symmetric superlattices with SrO-terminated SRO layers compared to formation energy of corresponding asymmetric superlattice for different misfit strains. The relaxation calculations were done using the WC parametrization of the general gradient approximation.

11.2 Asymmetric Structure

We analyzed the dependence on strain for the asymmetric $(SRO)_1(PTO)_5$ superlattice using the local density approximation. The strain-free in-plane lattice constants of bulk PTO , bulk SRO and bulk SRO are shown in table 11.3. We find that the strain conditions, corresponding to a STO substrate, stretch the PTO bulk unit cell and compress the SRO bulk unit cell for every parametrization of the exchange and correlation functional.

Under different epitaxial strain, the PTO and the SRO unit cell can be compressed or stretched respectively changing the physical properties of the system as shown in table 11.4.

First, we only consider the properties of the P_+ polarization state. The average tetragonality, the rumplings and therewith also the polarization increase when compressing the superlattice and they decrease when stretching the superlattice. This behavior is typical for ferroelectric materials.

The change in the polarization also leads to a change in the depolarizing field: A higher polarization causes more surface charges which can't be screened, and the field strength of the depolarizing field increases. Vice versa, a reduced polarization decreases the number of surface charges which can't be screened and the depolarizing field becomes weaker. Finding such a behavior, we can conclude that the change of the in-plane lattice constant does not have a strong effect on the screening properties of the metal.

Stretching (compressing) the superlattices also influences the existence and stability of the polarization state P_-. We find that the polarization state P_- is not stable for an in-plane lattice constant of $a = 3.87$Å and 3.92Å, but for an in-plane lattice constant of $a = 3.82$Å both polarization states are stable (see table 11.5). For a smaller in-plane lattice constant a both polarization states are stable because compressive misfit strain increases the ferroelectric instability. The double-well gets higher and the depolarizing field cannot switch the polarization any longer.

Structure	a[Å]	a[Å]	a[Å]
	LDA calculation	LSDA calculation	WC calculation
PTO	3.853	3.853	3.868
SRO	3.890	3.890	3.919
STO	3.870	3.870	3.905

Table 11.3: Unconstrained in-plane lattice constants of SRO, STO and PTO for different parametrization of the exchange and correlation functional

lattice constant a	$\left(\frac{c}{a}\right)_+$	$P_+\left[\frac{\mathrm{C}}{\mathrm{m}^2}\right]$	$(E_d)_{P_+}\left[\frac{\mathrm{eV}}{\mathrm{Bohr}}\right]$
3.77Å	1.090	0.668	$27.5 \cdot 10^{-3}$
3.82Å	1.046	0.477	$23.3 \cdot 10^{-3}$
3.87Å	1.018	0.358	$15.0 \cdot 10^{-3}$
3.92Å	0.991	0.277	$10.8 \cdot 10^{-3}$
3.97Å	0.970	0.257	$6.8 \cdot 10^{-3}$

Table 11.4: Tetragonality $\frac{c}{a}$, average layer polarization P and depolarizing field E_d for the asymmetric $(SRO)_1(PTO)_5$ structure in the polarization state P_+ constrained to different in-plane lattice constants a

Structure	$\left(\frac{c}{a}\right)_{P_+}$	$\left(\frac{c}{a}\right)_{P_-}$	$P_+\left[\frac{\mathrm{C}}{\mathrm{m}^2}\right]$	$P_-\left[\frac{\mathrm{C}}{\mathrm{m}^2}\right]$	$(E_d)_{P_+}\left[\frac{\mathrm{eV}}{\mathrm{Bohr}}\right]$	$(E_d)_{P_-}\left[\frac{\mathrm{eV}}{\mathrm{Bohr}}\right]$
$(\mathrm{SRO})_1(\mathrm{PTO})_5$ $a = 3.82$ Å	1.046	1.044	0.477	0.431	$23.3 \cdot 10^{-3}$	$23.9 \cdot 10^{-3}$

Table 11.5: Tetragonality $\frac{c}{a}$, average layer polarization P, depolarizing field E_d and average of direct bandgap for the asymmetric $(\mathrm{SRO})_1(\mathrm{PTO})_5$ structure constrained to $a = 3.82$ Å in the two polarization states P_+ and P_-

11.3 Symmetric Structure with SrO-terminated SRO

In the symmetric structures we see as well that compressive strain enhances the ferroelectricity whereas tensile strain reduces the ferroelectric behavior. In table 11.6 the average tetragonality, layer polarization and the field strength of the depolarizing field are given for a symmetric $(\mathrm{SRO})_1(\mathrm{PTO})_5$ structure constrained to different in-plane lattice constants a. Decreasing the in-plane lattice constant a results in an increase of the average tetragonality and the polarization. That's why the symmetric $(\mathrm{SRO})_1(\mathrm{PTO})_5$ structure is paraelectric for the in-plane lattice constants $a = 3.87$Å and $a = 3.92$Å but ferroelectric for $a = 3.82$Å.

lattice constant a	$\frac{c}{a}$	$P\left[\frac{\mathrm{C}}{\mathrm{m}^2}\right]$	$E_d\left[\frac{\mathrm{eV}}{\mathrm{Bohr}}\right]$
3.82Å	1.036	0.259	$17.3 \cdot 10^{-3}$
3.87Å	1.008	0.020	$1.7 \cdot 10^{-3}$
3.92Å	0.988	0.015	$1.6 \cdot 10^{-3}$

Table 11.6: Tetragonality $\frac{c}{a}$, average layer polarization P and depolarizing field E_d for the symmetric $(\mathrm{SRO})_1(\mathrm{PTO})_5$ superlattice with SrO-terminated SRO layers constrained to different in-plane lattice constants a

So far, we always constrained the superlattices to an ideal tetragonal structure. The authors of [4] showed that rotations and tilts of the oxygen octahedra can also play an important role in ferroelectric superlattices. In the next chapter, we thus relax our tetragonal constraints and allow rotations of the oxygen octahedra and analyze how the structures change under rotations of the oxygen octahedra.

Chapter 12

Rotations

12.1 Formation Energy

First, we again compare the formation energy of symmetric superlattices with SrO-terminated SRO layers to the formation energy of superlattices with asymmetric interfaces, but now some of the tetragonal symmetry constrains are lifted and rotations of the oxygen octahedra are allowed. The differences in formation energy are shown in table 12.1. We notice that the inclusion of rotations changes the stability of the structures. The $(STO)_1(PTO)_5$ superlattice is now most stable in the configuration with symmetric interfaces with SrO-terminated SRO layers. But the differences in formation energy are quite small and lie below the computational accuracy.

Structure	$\Delta E_{\text{formation}}$[eV] no rotations allowed	$\Delta E_{\text{formation}}$[eV] rotations included
$(STO)_1(PTO)_3$	-0.014	-0.003
$(STO)_1(PTO)_5$	0.009	-0.017

Table 12.1: Formation energy of symmetric superlattices with SrO-terminated SRO layers compared to formation energy of corresponding asymmetric superlattices using LDA calculations. In these calculations the tetragonal symmetry constraints were lifted and the oxygen octahedra were allowed to rotate. For comparison the differences in formation energy are also shown for the ideal tetragonal structures.

In the next section we study the rotations and their effects on the tetragonality and the rumplings in detail.

12.2 Asymmetric Structure

As described above in Section 3.3 the antiferrodistortive rotational modes are distinguished by the phase of the oxygen rotation of successive oxygen octahedra. To correctly account for the AFD_{zi} mode and the AFD_{zo} mode we use ferroelectric initial configurations upon which additional in phase and out of phase rotations of the oxygen octahedra were imposed.

For the $(SRO)_1(PTO)_3$ and the $(SRO)_1(PTO)_5$ superlattice we find that both rotational modes lower the total energy of the tetragonal ferroelectric state but relaxing the structures we find that the AFD_{zi} modes connected with in phase rotations of the oxygen octahedra can be unstable. In the $(SRO)_1(PTO)_5$

superlattice we do not find a configuration of the AFD_{zi} modes in which the maximal force component falls below 0.025eV/Å. In the $(SRO)_1(PTO)_3$ superlattice there is such configuration, but analysis of the rotational angles shows that more strict force conditions would probably also lead to a relaxation to the AFD_{zo} mode.

Figure 12.1 shows that the rumplings in structures with rotated oxygen octahedra become significantly smaller but we can still spot uniform rumplings in the $(SRO)_1(PTO)_5$ superlattice implying that it is still ferroelectric.This decrease of the rumplings causes a decrease of the polarization and could explain the large deviations between the experimental and theoretical polarizations discussed in Section 8.1 for the asymmetric structure.

The decreasing rumplings are accompanied by a decrease in tetragonality for the ferroelectric $(SRO)_1(PTO)_5$ structure as shown in table 12.2. The tetragonality of the paraelectric $(SRO)_1(PTO)_3$ structure increases under rotations of the oxygen octahedra.

The average rotation angle of the rotated oxygen octahedra in the different unit cells of the superlattice are given in table 12.3 for the AFD_{zo} mode. We find that the rotational distortions of the unit cells in the AFD_{zo} mode are similar for the two structures analyzed.

The antiferrodistortive rotations also change the band structure of the superlattice as the rotations correspond to a dimerization of the structure which is known to open a band gap.

Structure	$\frac{c}{a}$(tetragonal structure)	$\frac{c}{a}$(AFD_{zi} mode)	$\frac{c}{a}$(AFD_{zo} mode)
$(SRO)_1(PTO)_3$	1.0105	1.0119	1.0125
$(SRO)_1(PTO)_5$	1.0179	not stable	1.0159

Table 12.2: Average tetragonality for asymmetric $(SRO)_1(PTO)_3$ and $(SRO)_1(PTO)_5$ superlattice in different antiferrodistortive modes. LDA calculation

Structure	φ(PTO) [°]	φ(SRO) [°]
$(SRO)_1(PTO)_3$	6.0	8.3
$(SRO)_1(PTO)_5$	6.0	7.7

Table 12.3: Average rotation angles of the oxygen octahedra in the different unit cells of asymmetric SRO/PTO structures in the AFD_{zo} mode. LDA calculation

12.3 Symmetric Structure with SrO-terminated SRO

We also studied rotations in the symmetric structure with SrO-terminated SRO. For the $(SRO)_1(PTO)_3$ and the $(SRO)_1(PTO)_5$ superlattice with a symmetric interface we only find stable out of phase rotations which agree with the imposed force conditions. Comparing the forces in intermediate configurations between the AFD_{zi} mode and the AFD_{zo} mode confirms that the in phase rotations seem to be even less stable than in the asymmetric superlattice although the in phase rotation still lower the total energy.

Figure 12.2 shows that the $(SRO)_1(PTO)_3$ and the $(SRO)_1(PTO)_5$ structures still display vanishing rumplings corresponding to a paraelectric state. As seen above for the asymmetric $(SRO)_1(PTO)_3$ superlattice, table 12.4 indicates that the tetragonality of paraelectric states increases slightly under inclusion of rotations.

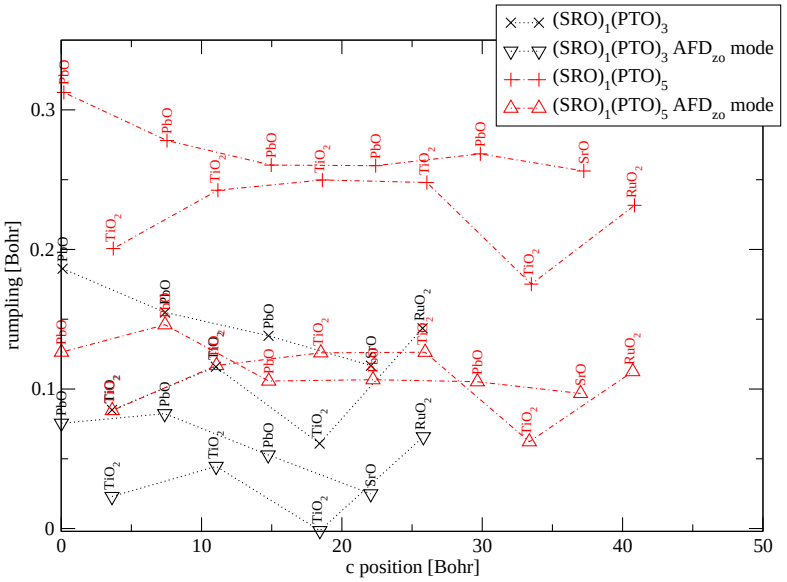

Figure 12.1: Comparison of layer rumplings between asymmetric structures in an ideal tetragonal configuration and structures with rotated oxygen octahedra . LDA calculation

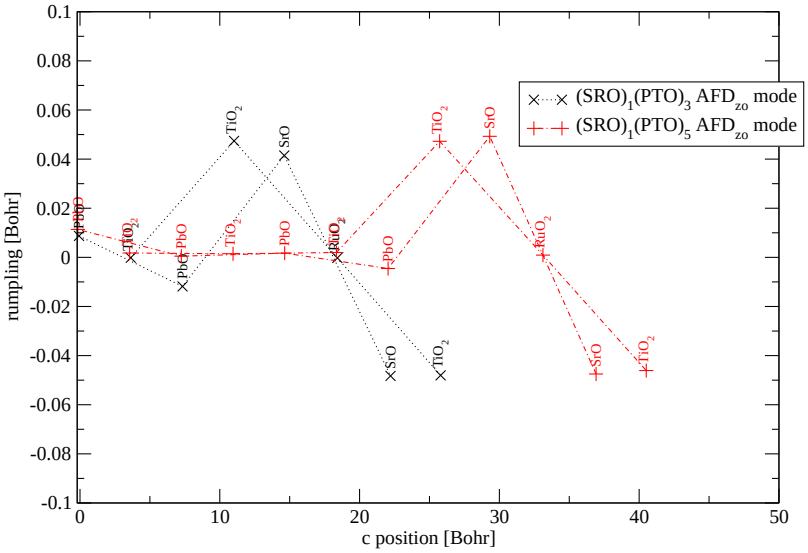

Figure 12.2: Comparison of layer rumplings between symmetric structures with SrO-terminated SRO in an ideal tetragonal configuration and structures with rotated oxygen octahedra. LDA calculation

We furthermore find that the average rotational distortions of the single perovskite unit cells in the superlattice are alike for the $(SRO)_1(PTO)_3$ and the $(SRO)_1(PTO)_5$ structures (see table 12.5), a behavior which we have already observed in the asymmetric superlatticea.

Structure	$\frac{c}{a}$(tetragonal structure)	$\frac{c}{a}$(AFD_{zi} mode)	$\frac{c}{a}$(AFD_{zo} mode)
$(SRO)_1(PTO)_3$	1.0075	not stable	1.0104
$(SRO)_1(PTO)_5$	1.0079	not stable	1.0105

Table 12.4: Average tetragonality $\frac{c}{a}$ for symmetric $(SRO)_1(PTO)_3$ and $(SRO)_1(PTO)_5$ superlattice with SrO-terminated SRO in different antiferrodistortive modes. LDA calculation

Structure	φ(PTO) [°]	φ(SRO) [°]	φ(STO) [°]
$(SRO)_1(PTO)_3$	5.3	9.0	4.2
$(SRO)_1(PTO)_5$	5.3	9.3	4.1

Table 12.5: Average rotation angles of the oxygen octahedra in the different unit cells of symmetric SRO/PTO structures with SrO-terminated SRO in the AFD_{zo} mode. LDA calculation

The constraints used in our calculations do not allow tiltings of the oxygen octahedra. This effect could lead to a further change in tetragonality, rumplings and polarization.

Chapter 13

Conclusion

Metal/ferroelectric $SrRuO_3/PbTiO_3$ superlattices were studied in this thesis. We identified three possible interface structures, an asymmetric interface, a symmetric interface with SrO-terminated SRO and a symmetric interface with RuO_2-terminated SRO, and tried to determine which interface is realized experimentally.

Analysis of the energetics, the structural and electrostatic properties of the symmetric structure with RuO_2-terminated SRO shows that this interface structure seems improbable as it is energetically unfavorable and the tetragonality and the polarization are overestimated by far compared to experiment.

For the asymmetric interface structure and the symmetric interface structure with SrO-terminated SRO the shape of the average tetragonality matches the experimental measurements. Making use of the different lattice constants of ferroelectric and paraelectric PTO and metallic SRO we found a model describing the shape of the tetragonality.

We also tried to match experimentally measured X-ray diffraction curves with curves calculated from the charge density of the different superlattices. The results of the comparison are unreliable as the theoretical calculations and the experimental measurements deviate in several orders of magnitude.

Studying the polarization of the asymmetric structures we find several phase transition. Structures with a high PTO volume fraction are ferroelectric but have an asymmetric double-well potential. Lowering the PTO volume fraction the $(SRO)_1(PTO)_5$ structure becomes self-poling with only one stable polarization state until the structure gets paraelectric for even smaller PTO volume fraction.

For the symmetric interfaces with SrO-terminated SRO we also find a phase transition between the paraelectric $(SRO)_1(PTO)_5$ and the ferroelectric $(SRO)_1(PTO)_6$ structure. The asymmetric polarization matches the experimentally measured polarization better.

The electronic structure of both interface configurations shows that in the case of a high PTO volume fraction, they are insulating in c direction. In x and y direction the SRO and one of the interfacial PTO unit cells are metallic, the bulk PTO unit cells remain insulating. The direct band gap is shown to depend on the PTO volume fraction.

We performed spin-polarized calculations studying the magnetic properties of the materials and found an interesting coupling between the polarization and the spin polarization in the asymmetric $(SRO)_2(PTO)_9$ superlattice.

The dependence of the superlattices on strain and rotational distortions was also analyzed. It was shown that the existence and magnitude of the ferroelectric instability depends sensitively on the imposed misfit strain. Including rotations of the oxygen octahedra we found that in phase antiferrodistortive rotations are

unstable in some structures. The stable out of phase rotations are shown to reduce the rumplings and the polarization of sample superlattices.

Summarizing, there is no really conclusive evidence that either the asymmetric structure or the symmetric structure with SrO-terminated SRO layers are the experimentally realized structures, although the asymmetric interface structure seems slightly more probable.

Avenues of future research include the analysis of magnetic properties which seem to be important in superlattices with more than one SRO unit cell.

The appearance of in-phase and out-of-phase rotations should also be studied for more structures, particularly in spin polarized systems. These studies would be useful, especially since differences in the rotational modes between different the interface structures could be used to determine the interface structure experimentally by performing X-ray diffraction in-plane.

Furthermore, it would be worthwhile to study how tiltings of the oxygen octahedra effect the properties of the superlattices. Another open question is how the inclusion of on-site Coulomb interactions in Ru changes the relaxations of the superlattices.

Experimentally, electrical measurements can be used to get further hints about the symmetry or asymmetry of the interface structure.

Bibliography

[1] Experimental data provided by S. Callori and M. Dawber.

[2] V. I. Anisimov, J. Zaanen, and O. K. Andersen. Band theory and Mott insulators: Hubbard U instead of Stoner I. *Phys. Rev. B*, 44(3):943–954, Jul 1991.

[3] M. Born and R. Oppenheimer. Zur Quantentheorie der Molekeln. *Ann. Phys. (Leipzig)*, 84(20):457, 1927.

[4] E. Bousquet, Ma. Dawber, N. Stucki, C. Lichtensteiger, P. Hermet, S. Gariglio, J.-M. Triscone, and P. Ghosez. Improper ferroelectricity in perovskite oxide artificial superlattices. *NATURE*, 452(7188):732–U4, APR 10 2008.

[5] D. M. Ceperley and B. J. Alder. Ground state of the electron gas by a stochastic method. *Phys. Rev. Lett.*, 45(7):566–569, Aug 1980.

[6] M. Dawber, N. Stucki, C. Lichtensteiger, S. Gariglio, P. Ghosez, and J.-M. Triscone. Tailoring the properties of artificially layered ferroelectric superlattices. *Advanced Materials*, 19(23):4153–4159, 2007.

[7] S. L. Dudarev, G. A. Botton, S. Y. Savrasov, C. J. Humphreys, and A. P. Sutton. Electron-energy-loss spectra and the structural stability of nickel oxide: An lsda+u study. *Phys. Rev. B*, 57(3):1505–1509, Jan 1998.

[8] A. García and D. Vanderbilt. First-principles study of stability and vibrational properties of tetragonal *pbtio*3. *Phys. Rev. B*, 54(6):3817–3824, Aug 1996.

[9] P. Hohenberg and W. Kohn. Inhomogeneous electron gas. *Phys. Rev.*, 136(3B):B864–B871, Nov 1964.

[10] J. Junquera, M. Zimmer, P. Ordejón, and Ph. Ghosez. First-principles calculation of the band offset at $BaO/BaTiO_3$ and $SrO/SrTiO_3$ interfaces. *Phys. Rev. B*, 67(15):155327, Apr 2003.

[11] R. D. King-Smith and D. Vanderbilt. Theory of polarization of crystalline solids. *Phys. Rev. B*, 47(3):1651–1654, Jan 1993.

[12] L. Kleinman and D. M. Bylander. Efficacious form for model pseudopotentials. *Phys. Rev. Lett.*, 48(20):1425–1428, May 1982.

[13] W. Kohn and L. J. Sham. Self-consistent equations including exchange and correlation effects. *Phys. Rev.*, 140(4A):A1133–A1138, Nov 1965.

[14] A. I. Liechtenstein, V. I. Anisimov, and J. Zaanen. Density-functional theory and strong interactions: Orbital ordering in Mott-Hubbard insulators. *Phys. Rev. B*, 52(8):R5467–R5470, Aug 1995.

[15] H. J. Monkhorst and J. D. Pack. Special points for brillouin-zone integrations. *Phys. Rev. B*, 13(12):5188–5192, Jun 1976.

[16] J. Moreno and J. M. Soler. Optimal meshes for integrals in real- and reciprocal-space unit cells. *Phys. Rev. B*, 45(24):13891–13898, Jun 1992.

[17] S.-G. Park, B. Magyari-Köpe, and Y. Nishi. Electronic correlation effects in reduced rutile TiO_2 within the LDA+U method. *Phys. Rev. B*, 82(11):115109, Sep 2010.

[18] J. P. Perdew and A. Zunger. Self-interaction correction to density-functional approximations for many-electron systems. *Phys. Rev. B*, 23(10):5048–5079, May 1981.

[19] M. Peressi, N. Binggeli, and A. Baldereschi. Band engineering at interfaces: theory and numerical experiments. *Journal of Physics D: Applied Physics*, 31(11):1273, 1998.

[20] K. Rabe, C.H. Ahn, and J.-M. Triscone. *Physics of ferroelectrics: a modern perspective*. Springer Verlag, 2007.

[21] K. Rabe, M. Dawber, C. Lichtensteiger, C.H. Ahn, and J.M. Triscone. Modern physics of ferroelectrics: Essential background. In *Physics of Ferroelectrics*, volume 105 of *Topics in Applied Physics*, pages 1–30. Springer Berlin / Heidelberg, 2007.

[22] G. Rijnders, D. H. A. Blank, J. Junghoon Choi, and C.-B Eom. Enhanced surface diffusion through termination conversion during epitaxial $SrRuO_3$ growth. *Applied Physics Letters*, 84(4):505–507, 2004.

[23] N. Sai, B. Meyer, and D. Vanderbilt. Compositional inversion symmetry breaking in ferroelectric perovskites. *Phys. Rev. Lett.*, 84(24):5636–5639, Jun 2000.

[24] J. M. Soler, E. Artacho, J. D. Gale, A. García, J. Junquera, P. Ordejón, and D. Sánchez-Portal. The SIESTA method for ab initio order- N materials simulation. *Journal of Physics: Condensed Matter*, 14(11):2745, 2002.

[25] M. Stengel, P. Aguado-Puente, N. A. Spaldin, and J. Junquera. Band alignment at metal/ferroelectric interfaces: Insights and artifacts from first principles. *Phys. Rev. B*, 83(23):235112, Jun 2011.

[26] N. Troullier and J. L. Martins. Efficient pseudopotentials for plane-wave calculations. *Phys. Rev. B*, 43:1993–2006, Jan 1991.

[27] M. Veríssimo-Alves, D. Bilc, P. García-Fernández, Ph. Ghosez, and J. Junquera. Highly confined 2D electron gas in $SrTiO_3$/$SrRuO_3$ superlattices. *APS Meeting Abstracts*, pages 34002–+, March 2011.

[28] Z. Wu and R. E. Cohen. More accurate generalized gradient approximation for solids. *Phys. Rev. B*, 73(23):235116, Jun 2006.

[29] A. T. Zayak, X. Huang, J. B. Neaton, and K. Rabe. Structural, electronic, and magnetic properties of $SrRuO_3$ under epitaxial strain. *Phys. Rev. B*, 74(9):094104, Sep 2006.